**Title:** Numerical Modeling of Self-Potential in Subsurface Reservoirs

**Author names and affiliations:**

Mutlaq Alarouj[1,2]

Amadi Ijioma[1]

Malcolm Thomas Graham[1,3]

Donald John MacAllister[1,4]

Matthew David Jackson[1]

[1]: Novel Reservoir Modelling and Simulation Group, DEPARTMENT OF EARTH SCIENCE AND ENGINEERING, Imperial College London, SW7 2AZ, United Kingdom

[2]: Kuwait Oil Company, 61008 Ahmadi, Kuwait

[3]: Now at: Atkins, Woodcote Grove, Ashley Road, Epsom, United Kingdom

[4]: Now at: British Geological Survey, Lyell Centre, Research Avenue South, Edinburgh

[1]

**Corresponding author:**

Mutlaq Alarouj

Email: m.alarouj17@imperial.ac.uk

**Link to the code:** https://github.com/mutlaqalarouj/SP-SOLVER.git

**Highlights:**

- Introduce a new tool for numerical simulating self-potential in subsurface reservoirs.
- Validate the accuracy of the new tool on single- and multiphase test cases.
- Demonstrate the application of the tool on an oil reservoir supported by water injection.

---

[1] **Authorship Statement:**

Mutlaq Alarouj: Wrote new sections of code handling variable polarity, LGRs, faults. Produced all results. Wrote first draft of paper.

Amadi Ijioma: Wrote early version of code, which this work further develops.

Malcolm Thomas Graham: Modified early version of code, to improve performance and stability.

Donald John MacAllister: Modified early version of code, which this work further develops.

Matthew David Jackson: Guidance on underlying physics, test solutions, case studies. Revised paper and figures.

## ABSTRACT

We report a new, open-source, MATLAB-based 3D code for numerically simulating the self-potential (SP) in subsurface reservoirs. The code works as a post-processor, using outputs from existing reservoir flow and transport simulators at a selected timestep to calculate the SP throughout the reservoir model. The material properties required to calculate the SP are user defined and may be constant or vary in each cell. The code solves the equations governing flow and transport of electrical charge and global charge conservation using a control-volume-finite-difference scheme. Electrical currents associated with the SP may spread beyond the reservoir model domain, and the code allows for the domain to be extended vertically and laterally to account for this. Here, we present the governing equations and the numerical method used and demonstrate application of the code using an example in which we predict the SP signals associated with oil production from a subsurface reservoir supported by water injection.



## Keywords

Self-Potential – Subsurface Reservoirs – Electrokinetic Potential – Exclusion-Diffusion potential – Thermoelectrical potential.


## 1. Introduction

The self-potential (SP) is a naturally occurring electrical potential that can be measured using electrodes at the Earth surface or in boreholes. Measurement of the SP is one of the oldest geophysical surveying methods with numerous applications (Jackson, 2015). Here, we focus on the use of SP to characterize and monitor water flow and the associated transport of salt species and/or heat in subsurface reservoirs. Numerous studies have investigated the SP associated with water flow in geothermal reservoirs (e.g., Corwin and Hoover, 1979; Revil and Pezard, 1998; Darnet et al., 2004) and during volcanic unrest (e.g., Zlotnicki and Nishida, 2003; Ishido, 2004; Finizola et al., 2004; Mauri et al., 2010); groundwater flow in aquifers (e.g., Fagerlund and Heinson, 2003; Titov et al., 2005; Linde et al., 2011; Jackson et al., 2012a; Hu et al., 2020); water flow in hydraulically active fractures (e.g., Revil and Pezard, 1998; Wishart et al., 2006, Roubinet et al., 2016, DesRoches et al. 2018; Jougnot et

al., 2020); contaminant transport in aquifers (e.g., Naudet et al., 2003, 2004; Minsley et al., 2007; Linde and Revil, 2007; Jougnot et al., 2015); saltwater intrusion in coastal aquifers (MacAllister et al., 2018; Graham et al., 2018), and water flow during hydrocarbon production (Saunders et al., 2008; Gulamali et al., 2011; Jackson et al., 2012b; Ijioma, 2016). The SP method has also been found very useful in mineral exploration (e.g., Caglar, 2000; Murthy et al., 2005; Abdelrahman et al., 2008; Di Maio et al., 2016) and more recently eco-hydrology (Voytek et al. 2019). However, prediction or interpretation of the SP in these subsurface environments is challenging as there may be several source mechanisms; moreover, flow and transport paths may be complicated by geological heterogeneity.

The aim of this paper is to report a new, open-source, MATLAB-based 3D code for numerically simulating the self-potential (SP) in subsurface reservoirs. Sources of SP in natural environments are numerous (e.g. Jackson, 2015) and here we restrict ourselves to the SP arising in partially or entirely water-saturated rocks in response to gradients in pressure (above hydrostatic, also termed water potential or head), water composition (salt concentration) and temperature. Numerous studies have described these SP source mechanisms (e.g. Ishido and Mizutani, 1981; Hunter, 1986; Revil et al., 1999a; Revil, 1999; Jackson et al., 2012b) and we provide a summary for the interested reader in Appendix A. A number of codes to simulate SP have been reported in the literature, but are limited to modelling the SP arising from pressure gradients in water saturated rocks (e.g., Soueid Ahmed et al, 2013; Rücker et al., 2017).

The new code works as a post-processor, taking outputs from existing reservoir flow and transport simulators at a selected timestep, and calculating the SP throughout the reservoir model using the simulated values of water saturation, pressure, concentration and temperature. The additional material parameters required to calculate the SP are user defined and may be constant or vary in each cell. Earlier versions of the code have been used previously in studies of saline intrusion into freshwater aquifers (MacAllister et al., 2018; Graham et al., 2018), and oil production from hydrocarbon reservoirs (Ijioma, 2016). However, the governing equations and method of solution

were not reported in these studies and the code has not hitherto been made available. Additional functionality included here also allows local grid refinement and simulation of SP in models of faulted reservoirs.

The code solves the equations governing flow and transport of electrical charge and global charge conservation using a control-volume-finite-difference scheme on the reservoir 3D mesh. Electrical currents associated with the SP may spread beyond the reservoir model domain, and the code allows for the domain to be extended vertically and laterally to account for this. The code can be used to predict the SP in a given reservoir, which is useful for (i) designing and implementing SP monitoring programmes, (ii) interpreting SP measurements from existing monitoring programmes, and (iii) understanding SP source mechanisms and the link between source mechanisms and flow and transport processes in the reservoir. Future applications could include inversion of SP measurements for reservoir properties of interest. The code can be used in a broad range of subsurface reservoir types including aquifers, geothermal reservoirs, targets for $CO_2$ storage, and hydrocarbon reservoirs. We present the governing equations and the numerical methods used to solve these and show that the code returns the correct solution for some simple test cases. We demonstrate application of the code using an example in which we predict the SP signals associated with oil production from a subsurface reservoir supported by water injection.

## 2. Governing equations

Assuming that water is the only charge-carrying fluid in the rock pore space, the general form of the constitutive equations used to describe the coupled problem can be written as (De Groot and Mazur, 1962)

$$\begin{pmatrix} j \\ q_w \\ h \\ v \end{pmatrix} = -\begin{bmatrix} \sigma_{fs}(S_w) & L_{EK} & L_{TE} & L_{ED} \\ L_{EK} & \frac{k k_{rw}(S_w)}{\mu_w} & A_1 & A_2 \\ L_{TE} & A_1 & K(S_w) & A_3 \\ L_{ED} & A_2 & A_3 & D(S_w) \end{bmatrix} \begin{bmatrix} \nabla U \\ \nabla \Phi \\ \nabla T \\ \nabla C_f \end{bmatrix} \quad (1)$$

where $j$ is the current density (A·m$^{-2}$), $\sigma_{fs}$ is the saturated rock electrical conductivity (S·m$^{-1}$), $S_w$ is the water saturation, $\nabla U$ is the electrical potential gradient (V·m$^{-1}$), $q_w$ is the water Darcy velocity (m·s$^{-1}$), $k$ is the rock absolute permeability (m$^2$), $k_{rw}$ is the relative permeability of water (fraction), $\mu_w$ is the dynamic viscosity of water (Pa·s), $\nabla\Phi$ is the pressure gradient above hydrostatic (or water potential in Pa·m$^{-1}$) where $\Phi = P_w - \rho_w g z$, $h$ is the heat flux (W·m$^{-2}$), $K$ is thermal conductivity (W·m$^{-1}$·K$^{-1}$), $\nabla T$ is the temperature gradient (K·m$^{-1}$), $v$ is the concentration flux (M·s$^{-1}$·m$^{-2}$), $D$ is the diffusion coefficient (m$^2$·s$^{-1}$), and $\nabla C_f$ is the concentration gradient (M·m$^{-1}$).

The on-diagonal terms in equation (1) appear in the well-known constitutive equations of Ohm's law, Darcy's law, Fourier's law, and Fick's law, respectively. The matrix is symmetric in linear thermodynamic systems in which fluxes are linear functions of thermodynamic forces ($\nabla U, \nabla\Phi, \nabla T$ and $\nabla C_f$) (De Groot and Mazur, 1962). The off-diagonal terms $L_{EK}$, $L_{ED}$ and $L_{TE}$ are the electrokinetic (EK), exclusion-diffusion (ED), and thermoelectrical (TE) cross-coupling terms, respectively. These terms describe the cross-coupling between electrical current and gradients in water potential, concentration, and temperature. The off-diagonal terms $A_1$ through $A_3$ represent cross-coupling terms governing the interactions between fluxes and gradients in electrical potential, water potential, temperature, and concentration that are not considered here.

The water flux, heat flux, and ion species flux can be calculated using existing commercial and academic reservoir flow and transport simulators such as Eclipse (Schlumberger, 2010), TOUGH2 (Pruess et al., 1999), IC-FERST (e.g. Gomes et al., 2016), the Matlab Reservoir Simulation Toolkit (MRST; Lie, 2019), SUTRA3D (Voss and Provost, 2002) and many more. These simulators neglect the cross-coupling terms $L$ because their impact on the calculated fluxes is negligible in the reservoirs of interest (Ishido and Mizutani, 1981; Wurmstich and Morgan, 1994; Revil et al., 1999b; Saunders et al., 2008). Given this, we can solve for the electrical current independently from the flux calculations in a 'post-processing' step, given the water potential, temperature, and concentration fields obtained from reservoir simulation.

## 3. Numerical solution

### *3.1. Electrodynamic Problem*

The equation governing transport of charge solved here, which includes the cross-coupling of current flow *j* with gradients in water potential, concentration and temperature, is extracted from equation (1)

$$j = -\sigma_{fs}(S_w)\nabla U - L_{EK}(S_w)\nabla\Phi - L_{ED}(S_w)\nabla C_f - L_{TE}(S_w)\nabla T \tag{2}$$

The coupling terms $L_x$ are functions of the electrical conductivity of the fluid saturated rock $\sigma_{fs}$ and the so-called coupling coefficients $c_x$ (Jackson et al., 2010)

$$L_x = \sigma_{fs} c_x \tag{3}$$

where subscript *x* represents EK, ED, or TE. The coupling coefficients ($c_x$) are petrophysical properties that relate electrical potential to gradients in water potential, concentration and temperature, and have units of $V{\cdot}Pa^{-1}$, $V{\cdot}M^{-1}$ and $V{\cdot}K^{-1}$, respectively.

Given that charge is conserved and assuming no net current flow across the boundaries of the model domain, then

$$\nabla . j = 0 \tag{4}$$

Combining equations (2) and (4) results in

$$\nabla.\left(\sigma_{fs}(S_w)\nabla U\right) = -\nabla.\left(L_{EK}(S_w)\nabla\Phi\right) - \nabla.\left(L_{EC}(S_w)\nabla C_f\right) - \nabla.\left(L_{TE}(S_w)\nabla T\right) \tag{5}$$

In order to solve for the SP $(U)$, equation (5) is discretized and solved for given values of saturation $(S_w)$, water potential $(\Phi)$, salt concentration $(C_f)$, and temperature $(T)$, and appropriate values of $\sigma_{fs}$, $L_{EK}$, $L_{ED}$, and $L_{TE}$. The $S_w$, $\Phi$, $C$, and $T$ data are obtained using any commercial or academic reservoir simulator. The resulting values usually represent discrete properties defined at the center of each grid cell of the model. To be consistent with this, we use a control-volume-finite-difference method to discretize and solve equation (5). We assume the simulator uses either a regular Cartesian

grid or a cornerpoint grid. Many commercial and academic reservoir simulation codes are compatible with these schemes for discretizing space (e.g. Schlumberger, 2010; Voss and Provost, 2002).

### *3.2. Discretization for Numerical Solution*

A one-dimensional system is used to explain the discretization (Figure 1). The domain is divided into grid cells with properties of interest defined at the center of each cell.

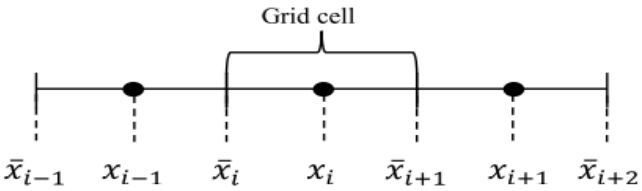


Figure 1: An example of a 1-D grid system

For simplicity, the numerical solution will be demonstrated considering only the EK potential; the procedure is the same to obtain the ED and TE potentials, replacing water potential $\Phi$ by concentration $C$ or temperature $T$, and $L_{EK}$ by $L_{ED}$ or $L_{TE}$ respectively.

For a non-boundary cell such as cell $i$ in Figure 1, equation (5) can be written as

$$\frac{d}{dx}\left(\sigma_{fs}\frac{dU}{dx} + L_{EK}\frac{d\Phi}{dx}\right) = 0 \tag{6}$$

Integrating equation (6) over cell $i$ results in

$$\int_{\bar{x}_i}^{\bar{x}_{i+1}} \frac{d}{dx}\left(\sigma_{fs}\frac{dU}{dx} + L_{EK}\frac{d\Phi}{dx}\right) dx$$

$$= \left[\left(\sigma_{fs_{\bar{x}_{i+1}}}\frac{dU}{dx}\right)_{\bar{x}_{i+1}} - \left(\sigma_{fs_{\bar{x}_i}}\frac{dU}{dx}\right)_{\bar{x}_i}\right] + \left[\left(L_{EK_{\bar{x}_{i+1}}}\frac{d\Phi}{dx}\right)_{\bar{x}_{i+1}} - \left(L_{EK_{\bar{x}_i}}\frac{d\Phi}{dx}\right)_{\bar{x}_i}\right] = 0 \tag{7}$$

Substituting $\frac{dU}{dx}$ and $\frac{d\Phi}{dx}$ with their central difference approximation leads to

$$\left[\left(\sigma_{fs_{\bar{x}_{i+1}}}\frac{U_{x_{i+1}}-U_{x_i}}{x_{i+1}-x_i}\right)-\left(\sigma_{fs_{\bar{x}_i}}\frac{U_{x_i}-U_{x_{i-1}}}{x_i-x_{i-1}}\right)\right]+\left[\left(L_{EK_{\bar{x}_{i+1}}}\frac{\Phi_{x_{i+1}}-\Phi_{x_i}}{x_{i+1}-x_i}\right)-\left(L_{EK_{\bar{x}_i}}\frac{\Phi_{x_i}-\Phi_{x_{i-1}}}{x_i-x_{i-1}}\right)\right]=0 \tag{8}$$

where variables $U_{xi}$ and $\emptyset_{xi}$ are identified at cell centers and $\sigma_{fs_{\bar{x}_i}}$ and $L_{EK_{\bar{x}_i}}$ are identified at cell faces. To further simplify equation (8), it can be written as

$$a_{\bar{x}_{i+1}}U_{x_{i+1}}+a_pU_{x_i}+a_{\bar{x}_{i-1}}U_{x_{i-1}}=b_{\bar{x}_{i+1}}\Phi_{x_{i+1}}+b_p\Phi_{x_i}+b_{\bar{x}_{i-1}}\Phi_{x_{i-1}} \tag{9}$$

where

$$a_{\bar{x}_{i+1}}=\frac{\sigma_{fs_{\bar{x}_{i+1}}}}{x_{i+1}-x_i}\quad(10a),\quad a_{\bar{x}_{i-1}}=\frac{\sigma_{fs_{\bar{x}_i}}}{x_i-x_{i-1}}\quad(10b)$$

$$a_p=-\frac{\sigma_{fs_{\bar{x}_{i+1}}}}{x_{i+1}-x_i}-\frac{\sigma_{fs_{\bar{x}_i}}}{x_i-x_{i-1}}=-\left(a_{\bar{x}_{i+1}}+a_{\bar{x}_{i-1}}\right)\ (10c)$$

$$b_{\bar{x}_{i+1}}=-\frac{L_{EK_{\bar{x}_{i+1}}}}{x_{i+1}-x_i}\quad(11a),\quad b_{\bar{x}_{i-1}}=-\frac{L_{EK_{\bar{x}_i}}}{x_i-x_{i-1}}\quad(11b)$$

$$b_p=\frac{L_{EK_{\bar{x}_{i+1}}}}{x_{i+1}-x_i}+\frac{L_{EK_{\bar{x}_i}}}{x_i-x_{i-1}}=-\left(b_{\bar{x}_{i+1}}+b_{\bar{x}_{i-1}}\right)\ (11c)$$

Equation (9) can be applied to all non-boundary cells. In boundary cells, we choose to set $\nabla U=0$ consistent with equation (4) which assumes no current enters or leaves the domain, by assigning virtual cells outside of the model boundary with the same electrical potential as the boundary cells.

### *3.3. Interface Properties*

Solution of equations 9 - 11 requires values for the properties at the interface between connected grid cells ($\sigma_{fs_{\bar{x}_{i+1}}}$ and $L_{EK_{\bar{x}_i}}$). Earlier approaches (Ijioma, 2016; Graham et al., 2018) used a harmonic average of the cell-center values, which is a reasonable assumption when the polarity of the coupling terms *L* for the two connected grid cells are the same. However, coupling terms can have variable

polarity, depending on the rock mineralogy, brine composition and mineral surface wettability (e.g. Leinov and Jackson 2014; Jackson et al. 2016). Thus, there is no guarantee that the coupling terms in each connected cell have the same polarity. When they have opposing polarity, the harmonic mean is not the appropriate averaging scheme to calculate the coupling term at the interface.

The new averaging scheme proposed in this paper uses conservation of charge to recognize that the total current (sum of the conduction and streaming currents) must be continuous at the interface to give

$$I_{\bar{x}_{i+1}} = -\sigma_{fs_{\bar{x}_{i+1}}} \nabla U_{\bar{x}_{i+1}} - L_{EK_{\bar{x}_{i+1}}} \nabla \Phi_{\bar{x}_{i+1}} \tag{12a}$$

$$I_{x_i} = -\sigma_{fs_{x_i}} \nabla U_{x_i} - L_{EK_{x_i}} \nabla \Phi_{x_i} \tag{12b}$$

$$I_{x_{i+1}} = -\sigma_{fs_{x_{i+1}}} \nabla U_{x_{i+1}} - L_{EK_{x_{i+1}}} \nabla \Phi_{x_{i+1}} \tag{12c}$$

where $x_i$ and $x_{i+1}$ are the location of the centers of grid cells $i$ and $i+1$, while $\bar{x}_{i+1}$ represent the location of the interface between the two grid cells (Figure 2). The subscripts in equation (12) reflect the location at which each property ($I$, $\sigma_{fs}$, $\nabla U$ or $L_{EK}$) is calculated. The first term on the right-hand side of equation (12) describes the conduction current while the second term represents the streaming current. The interface properties are calculated assuming continuous total current ($I_{\bar{x}_{i+1}} = I_{x_i} = I_{x_{i+1}}$). The final equations for calculating the interface properties are as follows (the derivation is shown in Appendix B)

$$\sigma_{fs_{\bar{x}_{i+1}}} = \frac{\sigma_{fs_{x_i}} \sigma_{fs_{x_{i+1}}} (x_{i+1} - x_i)}{(x_{i+1} - \bar{x}_{i+1}) \sigma_{fs_{x_i}} + (\bar{x}_{i+1} - x_i) \sigma_{fs_{x_{i+1}}}} \tag{13}$$

$$L_{EK_{\bar{x}_{i+1}}} = \frac{\sigma_{fs_{x_{i+1}}} L_{EK_{x_i}} (\bar{\mathrm{x}}_{i+1} - \mathrm{x}_i) + \sigma_{fs_{x_i}} L_{EK_{x_{i+1}}} (\mathrm{x}_{i+1} - \bar{\mathrm{x}}_{i+1})}{(x_{i+1} - \bar{x}_{i+1}) \sigma_{fs_{x_i}} + (\bar{x}_{i+1} - x_i) \sigma_{fs_{x_{i+1}}}} \tag{14}$$

The same formulations are used for the EC and TE potentials, replacing $L_{EK}$ and $\nabla\Phi$ by $L_{EC}$ and $\nabla C$ or $L_{TE}$ and $\nabla T$, respectively.

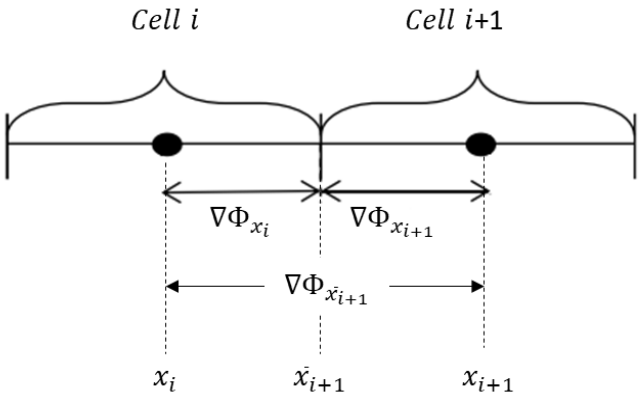


Figure 2: Variation in grid properties at the interface between two connected grid cells $i$ and $i+1$.

### *3.4. Fault Modeling*

Faults represent planar discontinuities in the rock mass across which rock units are offset. These discontinuities may modify fluid flow, and component and heat transport, depending on the properties of the fault (Cherubini et al., 2013; Knipe et al., 1998; Nurafiqah et al., 2019). Thus, they may modify charge transport in response to gradients in water potential, concentration and temperature. Faults may also modify the conduction currents that maintain overall electroneutrality. Hence, it is important to include them in reservoir models.

In many numerical models, the (cornerpoint) grid follows the geometry of the rock layers and the grid-cells are offset across fault planes in similar manner to the way in which the rocks are offset (e.g. Qu et al., 2015; Figure 4). Thus, cells juxtaposed across the fault are not logically neighbors and must be connected using so-called 'non-neighbor' connections (NNCs; e.g. Schlumberger, 2010).

In our example faulted grid (Figure 3b), grid cells $(i+1\,, j+2)$ and $(i+2\,, j)$ are juxtaposed across the fault and NNCs must be defined between these cells to model charge transport across the fault. We also need to identify new boundary cells resulting from the offset of the grid across the fault. In

our example faulted grid (Figure 3b), grid cell $(i+1\,, j+1)$ is a boundary cell. The SP solver is equipped with built-in functions to specify NNCs and boundary cells in order to correctly model charge transport. Modeling the charge flux into/out of each grid cell requires knowledge of all the grid cells connected to that cell. In our 2D example faulted grid (Figure 3b), grid cell $(i+1\,, j+2)$ has three neighbor connections with cells $(i+1\,, j+1), (i\,, j+2)$ and $(i+1\,, j+3)$ and one NNC with cell $(i+2\,, j)$.

Reservoir simulators that use this approach to represent faults typically generate a list of NNCs across fault surfaces. However, this list may be modified based on a cutoff transmissibility value (default or user defined) below which a NNC is deleted (Schlumberger, 2010). It is assumed that no fluid flow occurs across the deleted NNCs. However, there may be charge transport across these connections depending on the coupling terms and rock conductivity in the cells on each side. Hence, the NNC list calculated for fluid flow in a reservoir simulator may not be suitable for charge transport in the SP solver presented here. Hence, we have developed a bespoke function to generate the NNC list for the SP solver. The NNC list is generated based on the coordinates of the corner points of each cell, identifying any deviation in the grid geometry from the non-faulted case and generating NNC's across the boundaries of all juxtaposed cells (Figure 3). For the non-faulted case, the depths of the corner points at the interface between each two neighboring cells are the same, while in the presence of fault, layers offset across the fault interface, and hence, the depths of the corner points are not the same. The NNC list is generated by comparing the vertical offset in the depths of the corner points between all the cells across the fault interface. The layers offset may not be uniform resulting in multiple NNCs for one cell (figure 3b, grid Cell $(i+1\,, j+3)$). In this case, the interface properties calculated according equations (13) and (14) need to be corrected by multiplying by the ratio of the cross-sectional area in contact with each non-logical neighbor to the total cross-section area. The modeling approach described in this section deals with sealing faults only. However, faults could be hydraulically active; in this case, the SP may behave differently across the fault interface (e.g., Revil

and Pezard, 1998; Wishart et al., 2006, Roubinet et al., 2016, DesRoches et al. 2018; Jougnot et al., 2020). Modelling of the SP arising from flow in faults remains an area of active research.

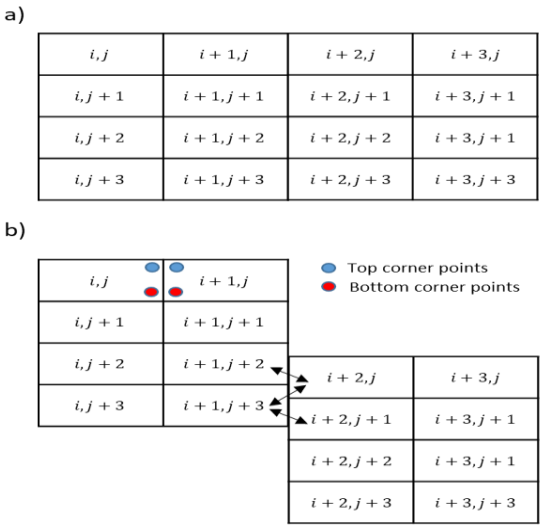


Figure 3: a) Example of an unfaulted 2D mesh. b) Example of a 2D mesh offset across a simple vertical fault. Arrows represent the non-neighbor connections that allow flow and transport between cells on opposite sides of the fault.

### *3.5. Local Grid Refinement*

In many models used to simulate SP monitoring scenarios, the grid resolution that provides a reasonable approximation of fluid flow and heat and mass transport is too coarse for accurate prediction of the SP, especially in the vicinity of SP monitoring locations where it may be necessary to capture changes in the hydrodynamic properties (e.g. water saturation, potential, concentration and temperature) at higher resolution. However, refining the grid across the entire model domain may be excessively computationally expensive. Instead, it may be sufficient to locally refine the grid (termed here 'Local Grid Refinement' (LGR) or 'child' model) around SP monitoring locations within the coarse ('parent') model (Ijioma, 2016; Figure 4). Many commercial and academic reservoir simulation codes allow LGR and we include functionality to allow these LGRs to be included in the SP solver.

We use a 'ghost-node' model-linking method (James et al. 2006) to couple the parent model with the LGR with appropriate LGR boundary conditions. The SP is simulated on the parent model, and the

electrical (SP, rock conductivity, coupling terms) and dynamic water saturation, potential, concentration and temperature) properties in each parent grid cell bordering the LGR are used to determine boundary conditions for simulating SP within the LGR. At the boundaries of the LGR, ghost cells similar in dimension to the LGR cells are placed in the parent cells (e.g. cells: $i_c - 1, j_c$ in Figure 4). Properties for these ghost cells are calculated by linearly interpolating values between the parent cells. For example, pressure and SP for ghost cell $i_c - 1, j_c$ (Figure 4) are interpolated between the parent cell hosting that ghost cell ($i, j + 1$ in Figure 4) and the parent cell hosting the LGR ($i + 1, j + 1$ in Figure 4). The electrodynamic model is then solved within the LGR subjected to the boundary conditions identified in the ghost cells.

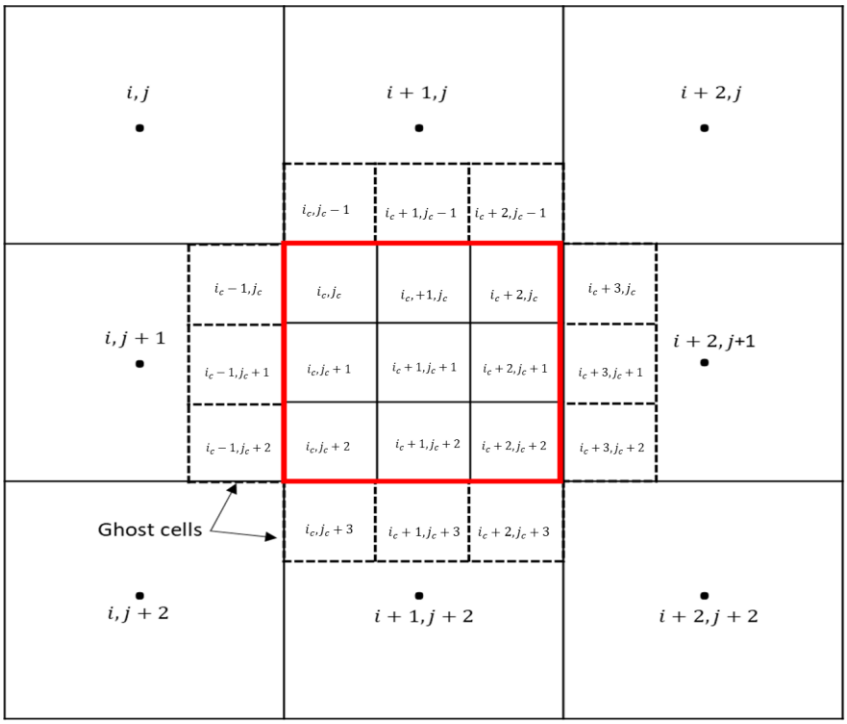


Figure 4: Example LGR within the parent grid (denoted by the red boundary). Cells outlined by dashed lines are the ghost cells introduced at the boundaries of the LGR. Subscript *c* (e.g., $i_c, j_c$) denotes cells within the LGR or ghost cells at the LGR boundaries.

### *3.6. Electrical Properties*

In order to solve equation (2), the concentration and temperature dependent material properties (rock conductivity ($\sigma_{fs}$) and coupling terms ($L_{EK}, L_{ED}, L_{TE}$)) must be specified. The operation of the

SP solver is independent of the models used to describe these material properties and the user can modify the code to implement their own preferred descriptions. We outline in Appendix C the approach we use in the code at present, and that was used to obtain the results presented.

### *3.7. Numerical Solution of the Linear System of Discretized Equations*

Equations 9-11 were used to write the formulation in matrix form considering all the grid cells in the system

$$Ax = By \tag{15}$$

where $A$ and $B$ are $n \times n$ sparse matrices (*n* is the total number of grid cells) comprising the $a$ and $b$ terms in equation (9), respectively. $x$ and $y$ are $n \times 1$ vectors representing the unknown EK, ED or TE potential and the known water potential, concentration, or temperature from the reservoir simulation, respectively.

MacAllister et al. (2018) and Graham et al. (2018) found that the solution obtained for $x$ using an iterative solver was unstable and highly sensitive to changes in the iterative solver tolerance, and Graham et al. (2018) recommended using a direct solver to obtain a stable solution. Therefore, we typically use a direct solver using the mldivide function in MATLAB (APPENDIX D) to solve for $x$ in equation (15). Although slower than the various iterative methods implemented in MATLAB, speed is not essential as we do not need to solve for the SP at numerous timesteps. We solve equation (15) for each of the EK, EC and TE potentials using the appropriate material properties and water potential, concentration or temperature as required. The total SP is obtained by summing over the EK, ED and TE potentials thus obtained.

As the SP signal is a potential difference between two points, the modelled SP is the difference in potential between a given location and that of a reference location, which is usually chosen at some distance above the reservoir layer.

## 4. Results

### *4.1. Model Validation*

A simple 1-D case was used to confirm that the code works correctly. The test case represents a sandstone reservoir measuring 200x100x50m with one oil/water production well and one water injection well. The ECLIPSE reservoir simulator was used to model two scenarios: first, water displacing water to represent single-phase flow and second, water displacing oil to represent two-phase flow.

First, we test the EK potential solver. Salinity and temperature were assumed to be constant across the reservoir (0.5 M/L and 80C°), so that EK potential is the only contributor to overall SP. We used a constant value of the EK coupling coefficient for the flow of water at fully water saturated conditions and at the residual non-wetting (oil) phase saturation ($C_{ek}(S_w = 1) = C_{ek}(S_w = 1 - S_{nwr}) = 2.5 \times 10^{-9}\ \mathrm{VPa}^{-1}$) (see Appendix C). For the two phase scenarios, we used fluid viscosities and relative permeability curves that yield a piston-like displacement such that oil is flowing at the irreducible water saturation ahead of the displacement front ($S_w = S_{wirr}$) and water is flowing at residual oil saturation behind the front ($S_w = 1 - S_{nwr}$). These material properties were used in the SP solver along with the outputs of the ECLIPSE reservoir simulator ($S_w, \Phi_w$) to predict the EK potential.

Results are shown in Figure 5 for both single- and multiphase flow scenarios. For the single-phase scenario, the correct solution yields a linear variation in EK potential from the inlet to the outlet boundary, with the most positive value adjacent to the inlet boundary where the water potential has the largest positive value. Moreover, a cross-plot of EK potential against water potential yields a linear relationship, with the gradient giving the EK coupling coefficient. We find that the SP solver predictions confirm the expected behavior irrespective of the grid resolution tested (Figure 5b), and the coupling coefficient obtained from the numerical solution is identical to the input value to high precision (Figure 5c).

For the multi-phase scenario, the correct solution yields constant EK potential ahead of the displacement front where there is no water flow, and a linear variation in EK potential from the inlet

to the location of the displacement front (see, for example, Figure 14 in Jackson, 2015). Moreover, a cross-plot of EK potential against water potential in the region behind the displacement front yields a linear relationship, with the gradient giving the EK coupling coefficient. As is well known (e.g. Aziz and Settari, 1979), numerical solutions of the multiphase displacement problem are highly dependent on grid resolution. However, as the grid is refined, the Eclipse simulator results converge to capture the correct sharp displacement front across which the water saturation changes sharply and the water phase potential changes gradient (Figure 5d,e). The SP solver results also converge to give the correct solution for the EK potential (Figure 5f); note that the rate of convergence is dominated by convergence of the Eclipse simulation results, not the SP solver itself. Behind the displacement front, the coupling coefficient obtained from the numerical solution approaches the input value as the grid is refined to high precision for the most refined case tested (Figure 5g). Thus, we have confidence that the SP solver returns correct solutions for the EK potential for both single and multiphase flow.

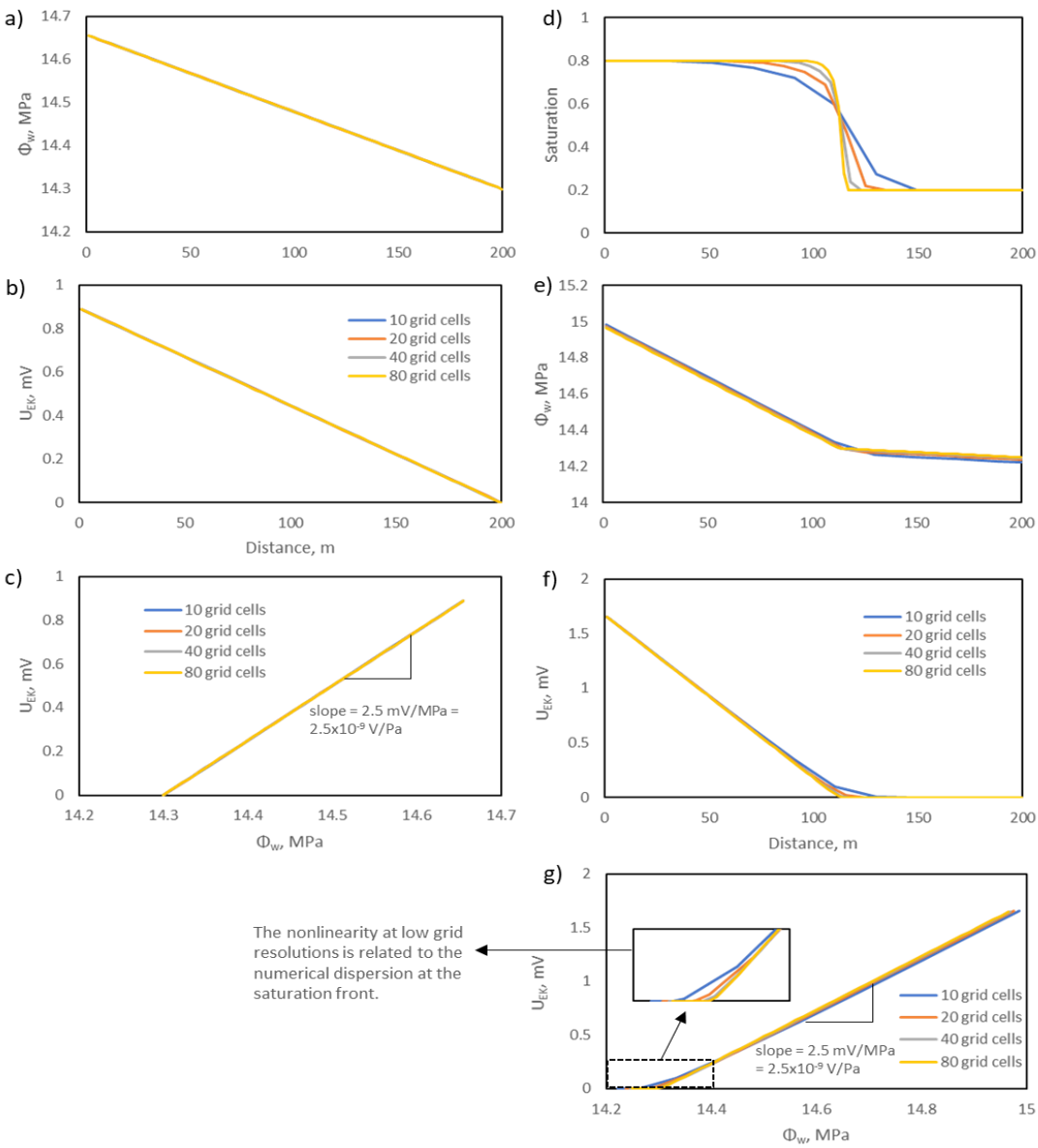


Figure 5: Numerical solutions from a single timestep of the EK validation model as a function of distance from the inlet to the outlet boundary. A) Water potential for the single-phase problem. b) EK potential for the single-phase problem. c) Cross-plots of EK potential against water potential for the single-phase problem. d) Water saturation for the multiphase problem. e) Water potential for the multiphase problem. f) EK potential for the multiphase problem. g) Cross-plots of EK potential against water potential for the multiphase problem. Lines in each plot correspond to different grid resolutions used in the model between the inlet and outlet boundaries.

To validate the ED potential solver, we modelled injection of lower salinity (ionic strength) brine ($C_{inj} = 0.5\mathrm{M/L}$) into a reservoir containing higher salinity brine ($C_{res} = 1\mathrm{M/L}$) using the ECLIPSE reservoir simulator. We assumed constant reservoir temperature of 80 C°. For the single-phase scenario, we assumed an exclusion efficiency of zero for the reservoir rock (similar to sandstone; see

Appendix C) and described the saturation dependence using equation (C.13) in the multi-phase scenario. These material properties together with the outputs of the ECLIPSE reservoir simulator ($S_w, C$) were used in the SP solver to predict the ED potential.

Results are shown in Figure 6 for both single- and multiphase flow scenarios. The correct solution yields constant ED potential behind the trailing edge of the salinity front and ahead of the leading edge of the salinity front (representing maximum and minimum values). Across the salinity front, the ED potential varies between these two values. We find that the SP solver predictions confirm the expected behavior. However, the grid resolution used significantly affects the modelled variation of the ED potential across salinity front, especially for the multiphase scenario (Figures 6b,f). This is primarily due to the grid-resolution-dependence of the solutions for salinity (and water saturation for the multiphase case) in the ECLIPSE simulator (Fig. 6a,d,e), rather than the solution for ED in our SP solver. As the grid is refined the solutions converge as expected, although high resolution is required for the multiphase case.

We confirm the validity of the SP solver solution by plotting the ED coupling coefficient values used as input to the SP code together with the simulated coefficients, determined using the ED potential determined by the solver and associated salinity (recalling $C_{ED} = \Delta U_{ED}/\Delta C_f$) for each neighboring cells as a function of distance from the inlet to the outlet boundary (Figure 6c,g). The coupling coefficient obtained from the numerical solution is the same as the input value to high precision. Therefore, we have confidence that the SP solver returns correct solutions for the ED potential for both single and multiphase flow.

Finally, to validate the TE potential solver, we modelled injection of cooler water ( $T_{inj} = 20^o\mathrm{C}$) into a hotter reservoir ( $T_{res} = 80^o\mathrm{C}$) using the ECLIPSE reservoir simulator. Salinity was assumed to be constant ($C_{res} = C_{inj} = 0.5\mathrm{M}$). We again assumed an exclusion efficiency of zero for the reservoir rock for the single-phase scenario and described the saturation dependence of the exclusion efficiency using equation (C.13) in the multi-phase scenario (Appendix C). These material properties together

with the outputs of the ECLIPSE reservoir simulator ($S_w, T$) were used in the SP solver to predict the TE potential.

Results are shown in Figure 7 for both single- and multiphase flow scenarios. The correct solution yields constant TE potential behind the trailing edge of the temperature front and ahead of the leading edge of the temperature front (representing maximum and minimum values). The TE potential varies between these two values across the temperature front. The SP solver predictions are consistent with the expected behavior. However, the variation of the TE potential across the temperature front is highly affected by the grid resolution, especially for the multiphase scenario (Figures 7b,f). This is mainly due to the grid-resolution-dependence of the solutions for temperature (and water saturation for the multiphase case) in the ECLIPSE simulator (Figure 7a,d,e), rather than the solution for TE in our SP solver. As expected, we find that the TE solutions converge as the grid is refined.

For the single-phase scenario, a cross-plot of TE potential against temperature should yield a linear relationship, with the gradient giving the TE coupling coefficient. We find that the coupling coefficient obtained from the numerical solution (0.188 mV/K; gradient from figure 7c) is identical to the input value (0.188 mV/K, according to equation (C.9); Appendix C) regardless of the grid resolution. This confirms the validity of the SP solver for TE solutions in the single-phase scenario. For the multi-phase scenario, the validity of the TE solution is confirmed by plotting the TE coupling coefficient values used as input to the SP code, together with the simulated coefficients determined using the TE potential determined by the solver and associated temperature (recalling $C_{TE} = \Delta U_{TE}/\Delta T$) for each pair of neighboring cells, as a function of distance from the inlet to the outlet boundary (Figure 7g). The coupling coefficient obtained from the numerical solution is the same as the input value to high precision. Thus, we also have confidence that the SP solver returns correct solutions for the TE potential in multiphase flow.

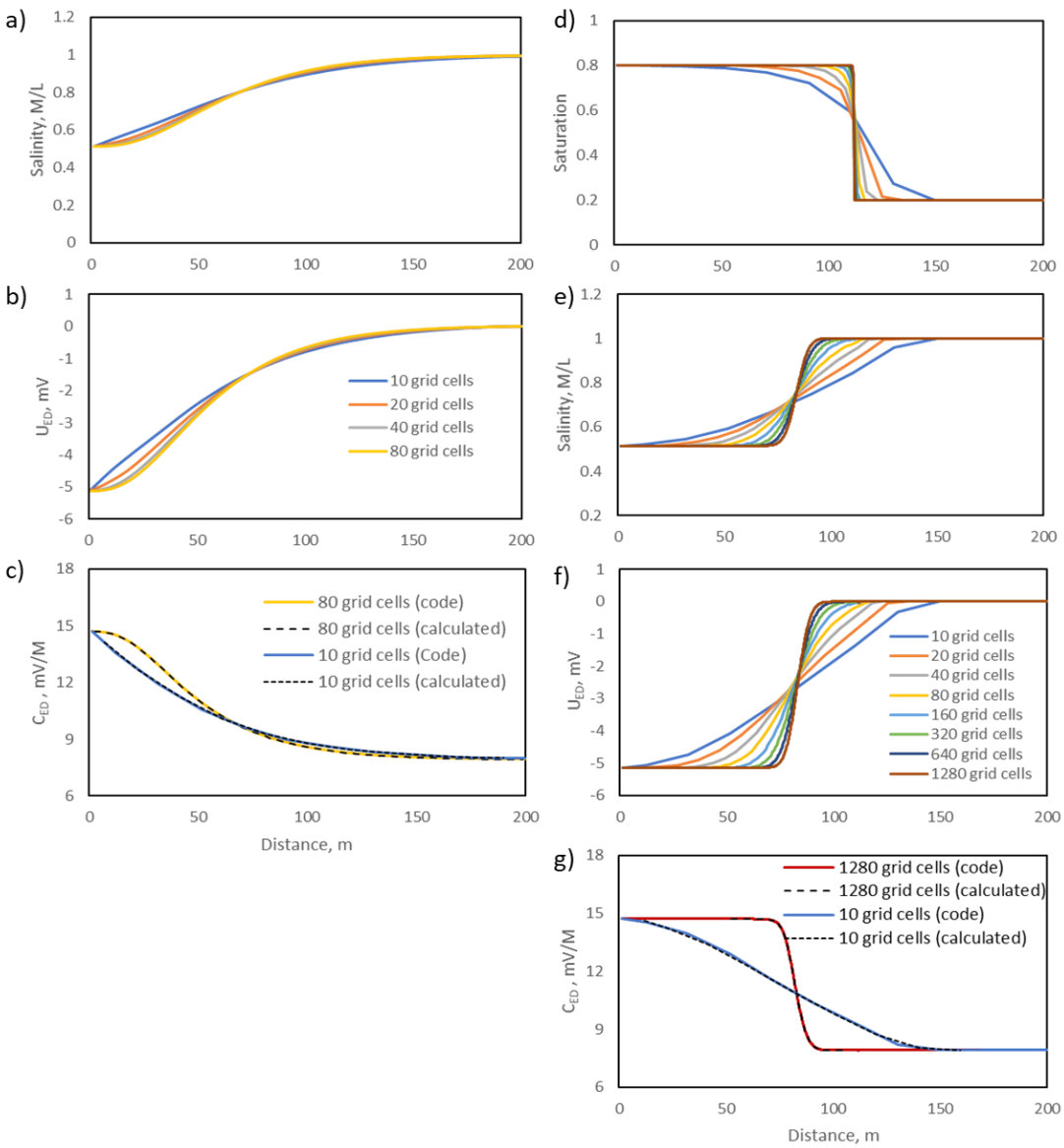


Figure 6: Numerical solutions from a single timestep of the ED validation model as a function of distance from the inlet to the outlet boundary. A) Water salinity for the single-phase problem. b) ED potential for the single-phase problem. c) ED coupling coefficient for the single-phase problem. d) Water saturation for the multiphase problem. e) Water salinity for the multiphase problem. f) ED potential for the multiphase problem. g) ED coupling coefficient for the multiphase problem. Lines in each plot correspond to different grid resolutions used in the model between the inlet and outlet boundaries.

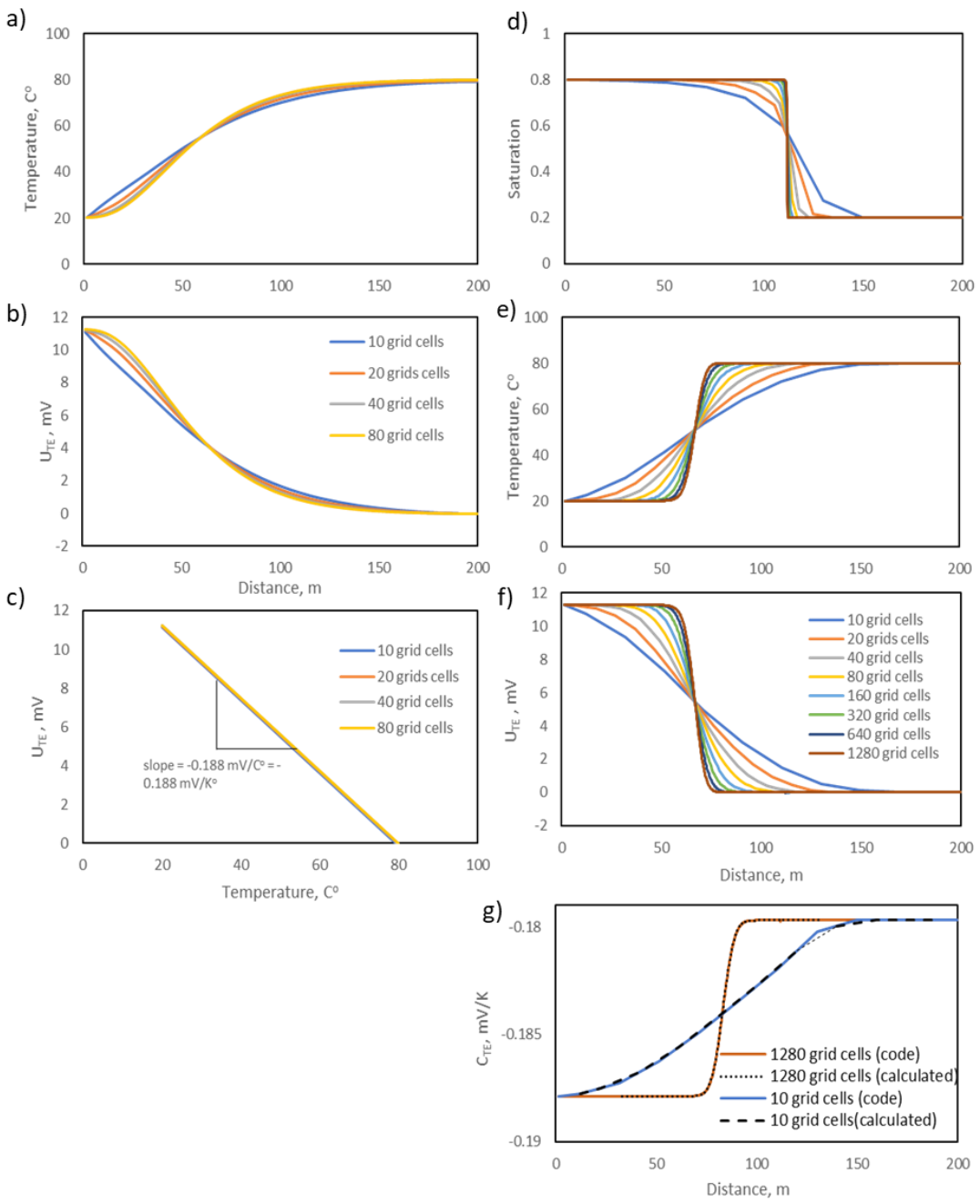


Figure 7: Numerical solutions from a single timestep of the TE validation model as a function of distance from the inlet to the outlet boundary. A) Temperature for the single-phase problem. b) TE potential for the single-phase problem. c) Cross-plots of TE potential against temperature for the single-phase problem. d) Water saturation for the multiphase problem. e) Temperature for the multiphase problem. f) TE potential for the multiphase problem. g) Cross-plots of TE potential against temperature for the multiphase problem. Lines in each plot correspond to different grid resolutions used in the model between the inlet and outlet boundaries.

### *4.2. Self-Potential in a Hydrocarbon Reservoir: Brugge Field Model*

The Brugge field case is a synthetic oil reservoir model comprising four stratigraphic layers: Schelde, Maas, Waal and Schie, from top to bottom (Figure 8; Table 1; Peters et al., 2010). The reservoir is initially saturated with oil and formation brine and overlies a water saturated aquifer (Figure 8; Table 2).

The production scenario considered here comprises 20 oil producers and 10 water injectors. The initial reservoir temperature and formation brine salinity were assumed to be 80 C° and 1 M/L, respectively. The injected brine was assumed to have lower temperature (30 C°) and salinity (0.5 M/L).

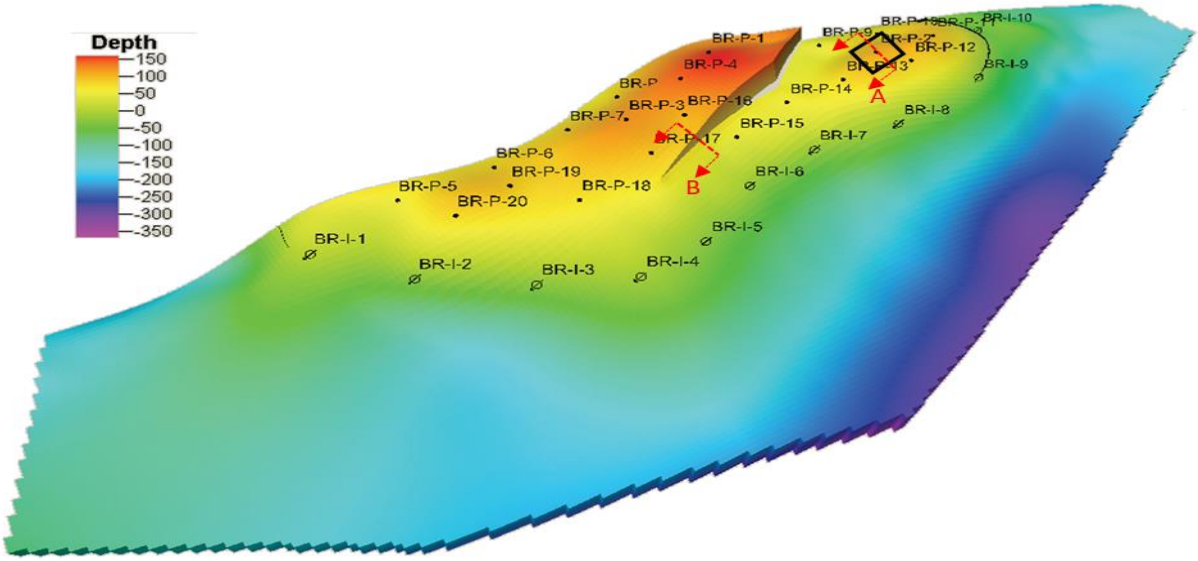


Figure 8: Structure of the Brugge field model showing the depth above and below the oil/water contact (in m) and the 30 wells (BR-P: production wells and BR-I: injection wells; Peters et al., 2010).

Table 1: Stratigraphy in the Brugge field model with main petrophysical properties (Peters et al., 2010).

| Reservoir formation | Average thickness, m | Average porosity, % | Average permeability, md | Average NTG, fraction |
|---|---|---|---|---|
| Schelde | 10 | 20.7 | 1105 | 0.6 |
| Maas | 20 | 19 | 90 | 0.88 |
| Waal | 26 | 24.1 | 814 | 0.97 |
| Schie | 5 | 19.4 | 36 | 0.77 |

Table 2: Rock and fluid used in the Brugge model.

| Properties | Water | Oil | Rock |
|---|---|---|---|
| Density, (Ibm/ft$^3$) | 62.2 | 56 | - |
| Compressibility, (1/psi) | $3x10^{-6}$ | $9.26x10^{-6}$ | $3.5x10^{-6}$ |
| Viscosity, (cp) | 1 | 1.294 | - |
| Irreducible water saturation | 0.252 | - | - |
| Critical water saturation | 0.29 | - | - |
| Residual oil saturation | 0.15 | - | - |
| Endpoint water relative permeability | 0.3 | - | - |
| Endpoint oil relative permeability | 0.8 | - | - |

The average grid size in the model is 120 × 120 × 10 m in the i,j,k directions respectively, which is too coarse to accurately simulate the SP in the vicinity of a well (Jackson et al. 2012a). Therefore, we placed LGRs of resolution 4 × 4 × 0.5 m around selected production wells to improve the predictions of the SP solver. Refining the grid to this level across the whole model would be computationally infeasible as the number of grid blocks required would be in excess of 1 billion. Hence, the LGR functionality in the SP solver is essential to obtain high resolution solutions around the wells of interest. A sensitivity study of the LGR resolution confirmed that the resolution used is sufficient to capture the SP solution. The refinement strategy that we follow is to refine in x,y and z until we observe conversion in the SP profile at the monitoring well of interest. The SP solver was used to here to predict the signals that might be recorded at a production well equipped with permanently installed downhole electrodes (Gulamali et al., 2011).

After running the dynamic simulation in ECLIPSE, the results were used as inputs for the SP solver. The model was modified in the solver to include electrically conductive, water saturated shale layers of thickness 70m above and below the reservoir. These shale layers represent the under- and over-burden and are required for the SP modelling as electrical currents may spread beyond the reservoir. The EK coupling coefficients in the reservoir were calculated according to Appendix C, but were zero in the shale layers as there is no flow. The ED and TE coupling coefficients were calculated following

the approach in Appendix C. The exclusion efficiency in the reservoir was assumed to vary between 0 to 1 as a function of saturation, while a constant value of 0.4 was used in the shale layers. The SP solver was used to simulate the EK, ED and TE contributions to the overall SP.

The results presented here focus on the new functionality of our SP solver. We begin by considering the benefits of the LGR functionality. The effect of increased grid resolution on the solution obtained is clearly observed (Figure 9). The LGR solutions yields a sharper saturation front as there is less numerical diffusion (compare Figure 9a, 9c), which significantly affects the simulated SP (compare Figure 9b, 9d). The higher resolution solution delivered by the LGR shows that the SP signal extends to the production well, ahead of the moving waterfront. Consequently, monitoring of the SP recorded at the well would provide useful information about the location of the waterfront as it approached the well (e.g. Gulamali et al., 2011; Saunders et al., 2012). In contrast, the coarse grid solution suggests that the SP would be featureless at the well (Figure 10). These results demonstrate the utility of the LGR modelling capability in our SP solver.

We next consider the modelling of faults. Figure 11 shows an example on the behavior of SP across fault (at cross-section B; figure 8). The fault shown in figure 11a is a sealing fault so there is no flow across the fault. In the simulation model grid, there are therefore no NNCs across the fault. However, the fault is electrically conductive so electrical current can flow across the fault. Consequently, the SP generated by flow on one side of the fault penetrates into the reservoir and bounding shales on the other side of the fault. These current fluxes are modelled using the NNCs generated by our SP solver. The results demonstrate the utility of the fault modelling capability in our SP solver.

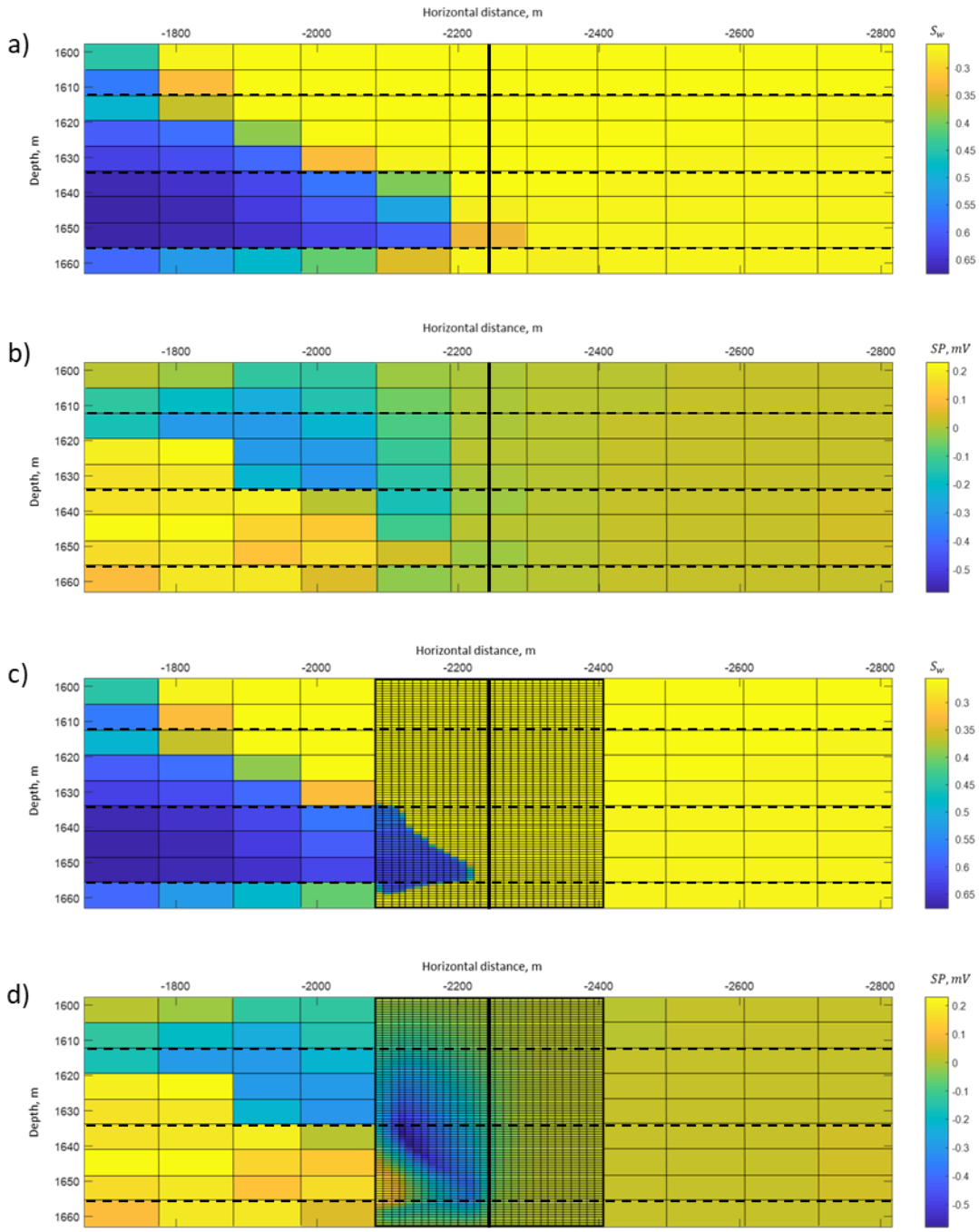


Figure 9: Vertical cross-sections along the plane A in Figure 10, showing a snapshot in time of (a) water saturation in the coarse model; (b) SP in the coarse model; (c) water saturation in the LGR model, and (d) SP in the LGR model. The dashed lines denote the 4 reservoir layers and the solid line represents the production well BR-P-2.

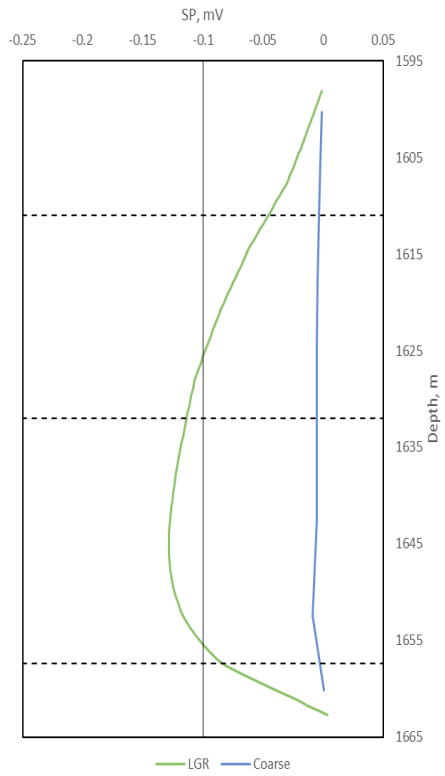


Figure 10: Predicted SP that would be measured along the well from the coarse and LGR models. The dashed lines denote the 4 reservoir layers and the solid line represents an assumed noise level of 0.1 mV.

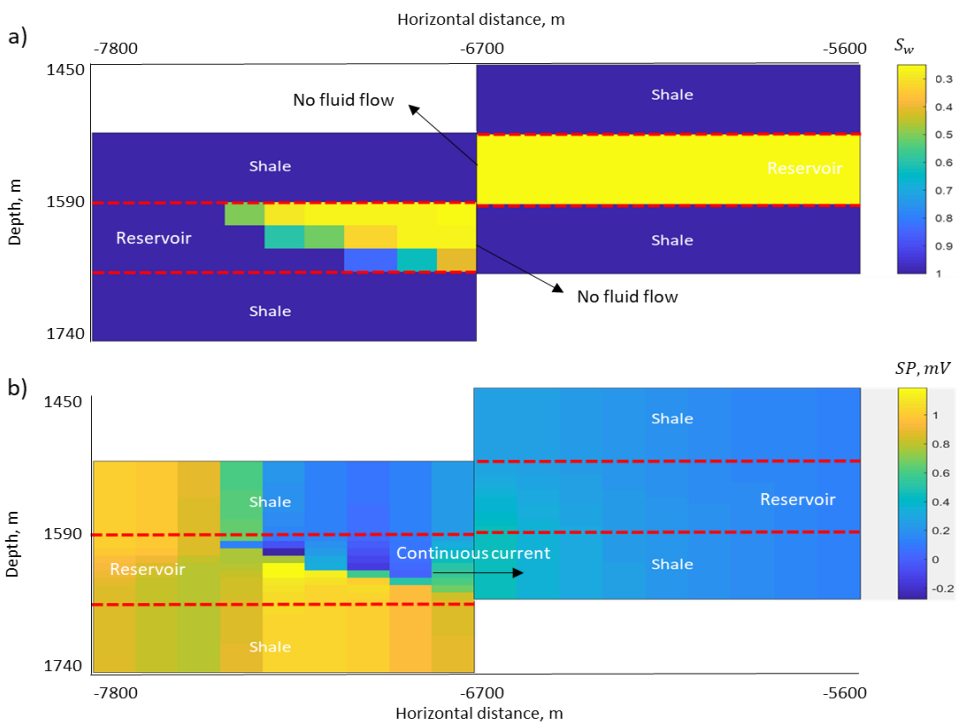

Figure 11: Vertical cross-sections along the plane B in Figure 10, showing a snapshot in time of (a) water saturation and (b) SP across the fault. The dashed lines denote the reservoir layers. There is no fluid flow across the fault, but there is current flow, so the SP generated by flow on one side of the fault penetrates into the reservoir and bounding shales on the other side of the fault.

## 5. Conclusions

We report a new, open-source, MATLAB-based code for numerically simulating the self-potential (SP) in subsurface reservoirs. The code works as a post-processor, using outputs from existing reservoir flow and transport simulators at a selected timestep to calculate the SP throughout the reservoir model. The material properties required to calculate the SP are user defined and may be constant or vary in each cell. The code solves the equations governing flow and transport of electrical charge and global charge conservation using a control-volume-finite-difference scheme.

We implement a new approach to calculate the current fluxes across grid-cell boundaries that can account for changes in polarity of the SP coupling coefficients. Electrical currents associated with the SP may spread beyond the reservoir model domain, and the code allows for the domain to be extended vertically and laterally to account for this. Accurate modelling of the SP may require locally fine grid resolution, and the code allows the use of local grid refinement in the reservoir flow or transport simulator and in the modelling of SP. Many subsurface reservoirs include faults, and the code allows the use of faulted grid, generating non-neighbor connections as necessary to model current flow across the fault. These non-neighbor connections may differ from those created in the reservoir flow or transport simulator, because the fault may act as a barrier to fluid flow or salt transport, but not as a barrier to electrical current.

We demonstrate that the SP solver produces accurate SP solutions for both single and multiphase flow in a series of test case, and then demonstrate its utility in predicting the SP signal that would be measured at a production well during oil production from a faulted sandstone reservoir bounded above and below by shales. Accurate simulation of the SP requires local grid refinement around the

production well, and must capture the flow of electrical current across the fault. The results suggest that downhole SP monitoring could be useful to identify and locate moving waterfronts in the reservoir.

**Computer code availability**

The code presented in this paper was developed in MATLAB. In order to run the code, the Parallel Computing toolbox should be installed. The code along with a detailed user manual can be downloaded from https://github.com/mutlaqalarouj/SP-SOLVER.git. Please cite this paper if you use the code. Test data for a simple hydrocarbon reservoir are also available in the same repository. The developers can be contacted via: m.alarouj17@imperial.ac.uk or m.d.jackson@imperial.ac.uk. Kuwait Oil Company are thanked for financial support. We thank TNO for making the Brugge Field dataset available.

## Appendix A

### Origin of the self-potential

Sources of SP in natural environments are numerous (e.g. Jackson, 2015). Here we restrict ourselves to the SP arising in partially or entirely water-saturated rocks in response to gradients in pressure (above hydrostatic, also termed water potential or head), water composition (salt concentration) and temperature.

Gradients in water potential cause water and other fluids to flow through the rock. The water drags with it an excess of electrical charge in the so-called 'electrical double layer' adjacent to the mineral surfaces, establishing a current termed the 'streaming current' (Hunter, 1986; Jackson et al., 2012b; Figure A.1a). However, the water is electrically conductive, so the charge dragged along by the flow cannot accumulate. Instead, a conduction current is established that *globally* balances the streaming current to ensure overall electroneutrality. The streaming current may not follow the same pathways as the conduction current, so *locally* they may not balance. From Ohm's Law, it is well known that a conduction current must be driven by an electrical potential difference; this potential difference is termed the 'electrokinetic' (EK) or 'streaming' potential and is the part of the SP that arises from gradients in water potential (Ishido and Mizutani, 1981; Revil et al., 1999a).

The water (brine) found in subsurface reservoirs contains dissolved, dissociated salt species. Gradients in salt species concentration cause ion transport by diffusion. However, the salt ions do not migrate at the same rate, causing an electrical charge separation that is countered by an electrical potential termed the 'diffusion potential'. The effect of the diffusion potential is to cause salt ions to migrate down the concentration gradient at the same rate irrespective of their mobility (Revil et al., 1999). If there is a concentration gradient across a rock with very small pore-size, then the electrical charge on the mineral surfaces may prevent ions of the same polarity from entering the pores; only ions with the opposing polarity can migrate down the concentration gradient, giving rise to an electrical potential termed the 'exclusion potential'. Together, these two sources of SP are termed

the ‘exclusion-diffusion’ (ED) or ‘electrochemical’ (EC) potential; this is the part of the SP that arises from concentration gradients (Revil, 1999; Jackson et al., 2012b; Figure A.1b).

Gradients in temperature also cause ion transport by diffusion, and the resulting electrical charge separation is countered by an electrical potential termed the ‘thermoelectric’ (TE) potential; this is the part of the SP that arises from temperature gradients (Jackson et al., 2012b). Hence, the overall SP modelled here comprises three components which sum to give the total SP: the electrokinetic (EK) potential, the exclusion-diffusion (ED) potential and the thermoelectrical (TE) potential, which arise in response to gradients in pressure, concentration and temperature, respectively.

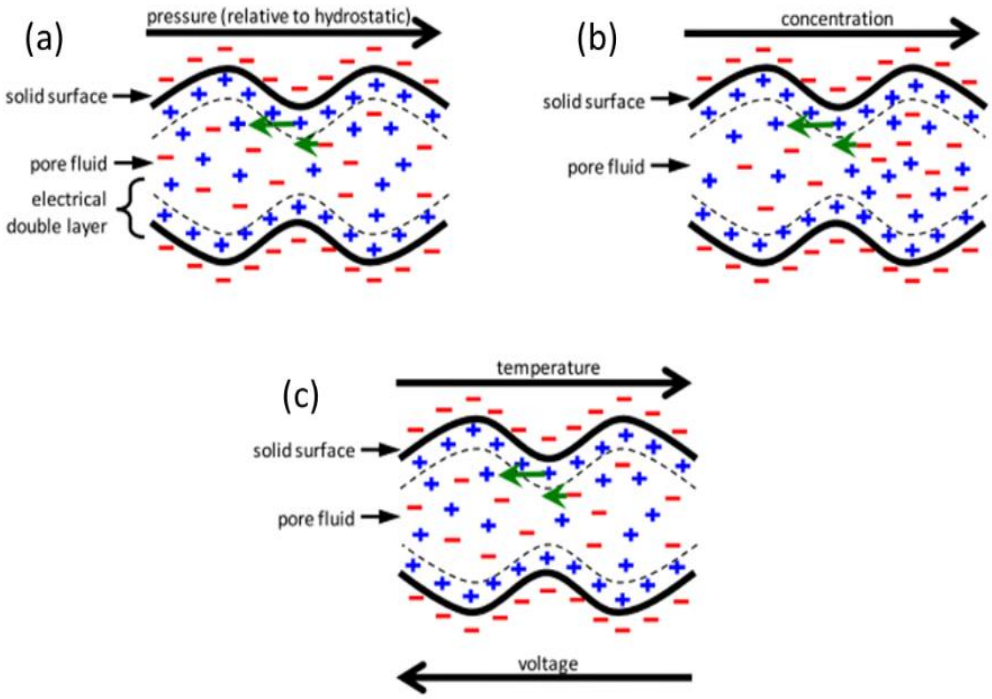


Figure A.1: Representation of charge separation due to (a) pressure, (b) concentration and (c) temperature gradients. The electrical double layer is denoted simply by the dashed line and here contains an excess of positive charge that balances the negative charge on the mineral surfaces (Jackson et al., 2012b). Ion transport is denoted by arrows.

## Appendix B

The procedures used to derive the formulas for the saturated rock conductivity and coupling terms at the interface between two grid cells are presented here. We consider only the electrokinetic potential (EK). The same steps were followed to derive the formulas for the electrochemical and thermoelectrical potentials. Referring to Figure 2, the total current at the interface is continuous.

$$I_{\bar{x}_{i+1}} = -\sigma_{fs_{\bar{x}_{i+1}}} \nabla U_{\bar{x}_{i+1}} - L_{EK_{\bar{x}_{i+1}}} \nabla \Phi_{\bar{x}_{i+1}} \qquad (B.1)$$

$\nabla U_{\bar{x}_{i+1}}$ can be approximated as

$$\nabla U_{\bar{x}_{i+1}} = \frac{\mathrm{U}_{x_{i+1}} - \mathrm{U}_{x_i}}{x_{i+1} - x_i} = \frac{\left(\mathrm{U}_{x_{i+1}} - \mathrm{U}_{\bar{x}_{i+1}}\right) + \left(\mathrm{U}_{\bar{x}_{i+1}} - \mathrm{U}_{x_i}\right)}{x_{i+1} - x_i} = \frac{\left(\mathrm{U}_{x_{i+1}} - \mathrm{U}_{\bar{x}_{i+1}}\right)}{x_{i+1} - x_i} + \frac{\left(\mathrm{U}_{\bar{x}_{i+1}} - \mathrm{U}_{x_i}\right)}{x_{i+1} - x_i}$$

(B.2)

Knowing that

$$\frac{x_{i+1} - x_i}{x_{i+1} - x_i} = \frac{x_{i+1} - \bar{x}_{i+1}}{x_{i+1} - x_i} + \frac{\bar{x}_{i+1} - x_i}{x_{i+1} - x_i} = m + n = 1 \qquad (B.3)$$

then $x_{i+1} - x_i$ can be written as

$$x_{i+1} - x_i = \frac{x_{i+1} - \bar{x}_{i+1}}{m} = \frac{\bar{x}_{i+1} - x_i}{n} \qquad (B.4)$$

Substituting equation (B.4) in equation (B.2)

$$\nabla U_{\bar{x}_{i+1}} = m \nabla U_{x_{i+1}} + n \nabla U_{x_i} \qquad (B.5)$$

Now, we apply equation (B.1) for cells $i\ and\ i+1$ as follows

$$I_{x_i} = -\sigma_{fs_{x_i}} \nabla U_{x_i} - L_{EK_{x_i}} \nabla \Phi_{x_i} \qquad (B.6)$$

$$I_{x_{i+1}} = -\sigma_{fs_{x_{i+1}}} \nabla U_{x_{i+1}} - L_{EK_{x_{i+1}}} \nabla \Phi_{x_{i+1}} \qquad (B.7)$$

Next, we rearrange equations (B.6) and (B.7) for $\nabla U_{x_i}$ & $\nabla U_{x_{i+1}}$

$$\nabla U_{x_i} = -\frac{I_{x_i}}{\sigma_{fs_{x_i}}} - \frac{L_{EK_{x_i}} \nabla \Phi_{x_i}}{\sigma_{fs_{x_i}}} \qquad (B.8)$$

$$\nabla U_{x_{i+1}} = -\frac{I_{x_{i+1}}}{\sigma_{fs_{x_{i+1}}}} - \frac{L_{EK_{x_{i+1}}} \nabla \Phi_{x_{i+1}}}{\sigma_{fs_{x_{i+1}}}} \qquad (B.9)$$

After that, we substitute equation (B.8) and equation (B.9) in equation (B.5)

$$\nabla U_{\bar{x}_{i+1}} = m\left(-\frac{I_{x_{i+1}}}{\sigma_{fs_{x_{i+1}}}} - \frac{L_{EK_{x_{i+1}}} \nabla \Phi_{x_{i+1}}}{\sigma_{fs_{x_{i+1}}}}\right) + n\left(-\frac{I_{x_i}}{\sigma_{fs_{x_i}}} - \frac{L_{EK_{x_i}} \nabla \Phi_{x_i}}{\sigma_{fs_{x_i}}}\right) \qquad (B.10)$$

Rearranging equation (B.10) results in

$$\nabla U_{\bar{x}_{i+1}} = -\left(\frac{nI_{x_i}}{\sigma_{fs_{x_i}}} + \frac{mI_{x_{i+1}}}{\sigma_{fs_{x_{i+1}}}}\right) - \left(\frac{nL_{EK_{x_i}} \nabla \Phi_{x_i}}{\sigma_{fs_{x_i}}} + \frac{mL_{EK_{x_{i+1}}} \nabla \Phi_{x_{i+1}}}{\sigma_{fs_{x_{i+1}}}}\right) \qquad (B.11)$$

Assuming the total current is continuous ($I_{x_i} = I_{x_{i+1}} = I_{\bar{x}_{i+1}}$), we can write equation (B.11) as

$$\nabla U_{\bar{x}_{i+1}} = -I_{\bar{x}_{i+1}}\left(\frac{n}{\sigma_{fs_{x_i}}} + \frac{m}{\sigma_{fs_{x_{i+1}}}}\right) - \left(\frac{nL_{EK_{x_i}} \nabla \Phi_{x_i}}{\sigma_{fs_{x_i}}} + \frac{mL_{EK_{x_{i+1}}} \nabla \Phi_{x_{i+1}}}{\sigma_{fs_{x_{i+1}}}}\right) \qquad (B.12)$$

$I_{\bar{x}_{i+1}}$ can be calculated by arranging equation (B.12) as follows

$$I_{\bar{x}_{i+1}} = -\frac{\nabla U_{\bar{x}_{i+1}}}{\frac{n}{\sigma_{fs_{x_i}}} + \frac{m}{\sigma_{fs_{x_{i+1}}}}} - \frac{\frac{nL_{EK_{x_i}} \nabla \Phi_{x_i}}{\sigma_{fs_{x_i}}} + \frac{mL_{EK_{x_{i+1}}} \nabla \Phi_{x_{i+1}}}{\sigma_{fs_{x_{i+1}}}}}{\frac{n}{\sigma_{fs_{x_i}}} + \frac{m}{\sigma_{fs_{x_{i+1}}}}} \qquad (B.13)$$

The first component of equation (B.11) is the conduction current related to the naturally occurring SP ($\nabla U$), while the second component is the streaming current related to the pressure gradient ($\nabla \Phi$).

The saturated rock conductivity ($\sigma_{fs_{\bar{x}_{i+1}}}$) at the interface between grid cells $i$ and $i+1$ can be calculated by equating the first term of equation (B.1) and (B.13) as follows

$$\sigma_{fs_{\bar{x}_{i+1}}} = \frac{1}{\frac{n}{\sigma_{fs_{x_i}}} + \frac{m}{\sigma_{fs_{x_{i+1}}}}} == \frac{\sigma_{fs_{x_i}}\sigma_{fs_{x_{i+1}}}(x_{i+1} - x_i)}{(x_{i+1} - \bar{x}_{i+1})\sigma_{fs_{x_i}} + (\bar{x}_{i+1} - x_i)\sigma_{fs_{x_{i+1}}}} \qquad (B.14)$$

For the coupling term at the interface ($L_{EK_{\bar{x}_{i+1}}}$), we need to equate the second terms of equations (B.1) and (B.13) as

$$L_{EK_{\bar{x}_{i+1}}}\nabla\Phi_{\bar{x}_{i+1}} = \frac{\frac{nL_{EK_{x_i}}\nabla\Phi_{x_i}}{\sigma_{fs_{x_i}}} + \frac{mL_{EK_{x_{i+1}}}\nabla\Phi_{x_{i+1}}}{\sigma_{fs_{x_{i+1}}}}}{\frac{n}{\sigma_{fs_{x_i}}} + \frac{m}{\sigma_{fs_{x_{i+1}}}}} \qquad (B.15)$$

Rearranging equation (B.14) considering the numerical approximation of $\nabla\Phi_{x_i}$, $\nabla\Phi_{x_{i+1}}$, and $\nabla\Phi_{\bar{x}_{i+1}}$, and considering the definition of $m\ and\ n$ for equation (B.3), equation (B.15) can be written as

$$L_{EK_{\bar{x}_{i+1}}}\left(\Phi_{x_{i+1}} - \Phi_{x_i}\right) = \frac{\sigma_{fs_{x_{i+1}}}L_{EK_{x_i}}\left(\Phi_{\bar{x}_{i+1}} - \Phi_{x_i}\right) + \sigma_{fs_{x_i}}L_{EK_{x_{i+1}}}\left(\Phi_{x_{i+1}} - \Phi_{\bar{x}_{i+1}}\right)}{m\sigma_{fs_{x_i}} + n\sigma_{fs_{x_{i+1}}}} \qquad (B.16)$$

The only unknown value in equation (B.16) is $\Phi_{x_{i+1}}$, which the water potential at the interface between cells $i\ and\ i+1$. This value can be approximated by linear interpolation. The final formula of $L_{EK_{\bar{x}_{i+1}}}$ can be written as

$$L_{EK_{\bar{x}_{i+1}}} = \frac{\sigma_{fs_{x_{i+1}}}L_{EK_{x_i}}(\bar{\mathrm{x}}_{i+1} - \mathrm{x}_i) + \sigma_{fs_{x_i}}L_{EK_{x_{i+1}}}(\mathrm{x}_{i+1} - \bar{\mathrm{x}}_{i+1})}{(x_{i+1} - \bar{x}_{i+1})\sigma_{fs_{x_i}} + (\bar{x}_{i+1} - x_i)\sigma_{fs_{x_{i+1}}}} \qquad (B.17)$$

which is the same as equation (14) presented in the main text.

## Appendix C

In order to solve equation (2), the concentration and temperature dependent material properties (rock conductivity ($\sigma_{fs}$) and coupling terms ($L_{EK}, L_{ED}, L_{TE}$)) must be specified. The operation of the SP solver is independent of the models used to describe these material properties and the user can modify the code to implement their own preferred descriptions. Here we outline the approach we use in the code at present, and that was used to obtain the results presented.

The saturated rock conductivity is calculated using the well-known Archie's equation (Glover et al., 2000)

$$\sigma_{fs} = \emptyset^m \sigma_w S_w^n \qquad (C.1)$$

where $\emptyset$ is the porosity, *m* is the cementation exponent, $S_w$ is the water saturation, *n* is the saturation exponent, and $\sigma_w$ is the water conductivity (S/m). The water conductivity is calculated as a function of the salt concentration (*C*, M/L) and temperature (*T*, °C) using (Sen and Goode, 1992; Figure 6a)

$$\sigma_w = (5.6 + 0.27T - 1.5 \times 10^{-4}T^2)C_f - \frac{2.36 + 0.099T}{1 + 0.214C_f^{0.5}} C_f^{1.5} \qquad (C.2)$$

The coupling terms ($L_{EK}, L_{ED}, L_{TE}$) are functions of the rock conductivity and the associated coupling coefficients ($C_{EK}, C_{ED}, C_{TE}$). First, we will consider the electrokinetic coupling coefficient ($C_{EK}$). A number of experimental and theoretical studies have characterized the electrokinetic coupling coefficients for sandstones (e.g. Revil and Cerepi, 2004; Jaafar et al., 2009; Vinogradov et al., 2010; Glover et al., 2012; Walker et al., 2014; Vinogradov and Jackson, 2015; Esmaeili et al., 2016; Vinogradov et al., 2018; Walker and Glover, 2018; Glover, 2018; Li et al., 2018) and carbonates ( e.g. Jackson and Vinogradov, 2012; Chen et al., 2014; Alroudhan et al., 2016; Jackson et al., 2016; Al Mahrouqi et al., 2017; Ghommem et al., 2018; Collini et al., 2020). Here, we focus on sandstones although, as mentioned above, the $C_{EK}$ model used here can easily be modified or changed for other rock types.

Most of the published EK coupling coefficient data for sandstones were obtained for fully saturated ($S_w = 1$) conditions at laboratory temperature. We describe the observed trend with brine concentration (ionic strength) using (Vinogradov et al., 2010)

$$C_{EK}(S_w = 1) = -1.36 C_f^{-0.9123} \times 10^{-9} \qquad (C.3)$$

Equation (C.3) fits data measured in sandstone samples saturated with simple monovalent NaCl brines (Figure C.1b). Alternative expressions can easily be implemented in the code. We note that the limited data available suggest that the EK coupling coefficient for complex natural brines is smaller in magnitude for a given ionic strength compared to the values in monovalent brines shown in Figure C.1b (Vinogradov et al., 2018; Li et al., 2018). We neglect any temperature dependence of the EK coupling coefficient, consistent with the findings of previous studies that show it is approximately independent of temperature over the range of 20-120°C in brines of moderate to high ionic strength (Reppert and Morgan, 2003a, 2003b; Vinogradov and Jackson, 2015; Vinogradov et al., 2018).

In reservoirs partially saturated with water, such as oil and gas reservoirs and unconfined aquifers, the EK coupling coefficient is a function of water saturation. A number of studies have measured and/or modelled the relationship between coupling coefficient and water saturation in sandstone and carbonate rocks (Wurmstich and Morgan, 1994; Perrier and Morat, 2000; Guichet et al., 2003; Revil and Cerepi, 2004; Linde et al., 2007; Revil et al., 2007; Jackson, 2010; Vinogradov and Jackson, 2011; Gulamali, et al., 2012; Allègre et al., 2012; Jougnot et al., 2012; Jackson et al. 2012a; Zhang et al., 2017; Soldi et al., 2019). Here, we assume water is the wetting phase and follow the approach of Jackson et al. (2012b) to describe the saturation dependence of the coupling coefficient, noting that it is trivial to replace this model in the code with other published or new models. We assume that the coupling coefficient at the residual non-wetting phase saturation is the same as that at fully water saturated conditions, and define a saturation-dependent relative coupling coefficient ($C_{r_{EK}}$)

$$C_{rEK} = S_{wn}^{0.6} \qquad (C.4)$$

$$S_{wn} = \frac{S_w - S_{wirr}}{1 - S_{wirr} - S_{nwr}} \qquad (C.5)$$

$$C_{EK}(S_w) = C_{EK}|_{S_w=1} C_{rEK}(S_w) \qquad (C.6)$$

where $S_{wn}$ is the normalized water saturation, $S_{wirr}$ is the irreducible water saturation and $S_{nwr}$ is the residual non-wetting phase saturation. Equation (C.4) was chosen to match the results of a bundle capillary tube model presented by Jackson (2010) and experimental data obtained by Revil and Cerepi (2004).

Next, we consider the ED and TE coupling coefficients. ED and TE potentials have two end-member cases: pure exclusion and pure diffusion (Figure C.1c,d). The salinity and temperature dependence of the ED and TE coupling coefficients for pure exclusion and pure diffusion cases are given by (Revil, 1999; Jackson et al., 2012a; Leinov and Jackson, 2014; Jackson, 2015)

$$C_{ED}|_{ed} = -8.61 \times 10^{-2} \frac{(2t_{Na} - 1)T}{C_f} \quad mV.M^{-1} \qquad (C.7)$$

$$C_{ED}|_{ee} = -8.61 \times 10^{-2} \frac{T}{C_f} \quad mV.M^{-1} \qquad (C.8)$$

$$C_{TE}|_{ed} = -1.984 \times 10^{-1}(2t_{Na} - 1)\left(logC_f\right) + 1.059t_{Na} - 5.673 \times 10^{-1} \quad mV.K^{-1} \qquad (C.9)$$

$$C_{TE}|_{ee} = -1.984 \times 10^{-1}\left(logC_f\right) + 5.953 \times 10^{-1} \quad mV.K^{-1} \qquad (C.10)$$

$$t_{Na} = \begin{cases} 0.39 & C < 0.09\ M \\ 3.66 \times 10^{-1} - 2.12 \times 10^{-2}\left(log_{10}C_f\right) & C > 0.09\ M \end{cases} \qquad (C.11)$$

where subscripts $ed$ and $ee$ refers to pure diffusion and pure exclusion cases, respectively. $t_{Na}$ is the macroscopic Hittorf transport number for the Na ions, noting that this approach assumes charge transport is dominated by $Na^+$ and $Cl^-$ ions arising from the dissociation of NaCl, which is a reasonable assumption for subsurface reservoirs (Numbere et al., 1977; Angelis, 2005). Experimentally measured data on shales, sandstones and carbonate rock samples lie between the pure exclusion and diffusion limits for both the ED and TE potentials (Figure C.1c,d). Note that the effect of temperature on the TE

coupling coefficient is neglected in equations (C.9) and (C.10) because of the small variation of the TE coefficient (<8%) over the temperature range 20 - 120 C° (Jackson et al., 2012b).

The relative contribution of the exclusion and diffusion components of the EC and TE potentials can be defined by a dimensionless number termed the 'exclusion efficiency' ($\varepsilon$). An exclusion efficiency of unity corresponds to an exclusion-dominated ED or TE potential, while an efficiency of zero corresponds to a diffusion-dominated ED or TE potential (Leinov and Jackson, 2014). The ED and TE coupling coefficients are modelled as a function of exclusion efficiency as (Graham et al.,2018)

$$C_x = \varepsilon_x \cdot (C_x|_{ee} - C_x|_{ed}) + C_x|_{ed} \qquad (C.12)$$

where subscript x refers to either ED or TC. Unlike EK potential, ED and TE potentials can be generated across impermeable layers if there is a concentration or temperature gradient, even though there is no water flow. The exclusion efficiency in fully saturated rocks varies with the rock pore-size (see REFS) so an appropriate value of exclusion efficiency value must be assigned to each rock type; for example, MacAllister et al. (2019) measured values of $\varepsilon$=0-0.1 and $\varepsilon$=0.3-0.4 for sandstones and shales, respectively.

In reservoirs partially saturated with water, the exclusion efficiency also varies with water saturation (Ortiz et al., 1973). We use here the approach described by Ortiz et al. (1973) to model the behavior of the exclusion efficiency at the saturation endpoints ($S_w = S_{wirr}$ and $S_w = 1 - S_{nwr}$). At low water saturation, Ortiz et al. (1973) suggested that the excess charge is confined to thin water films and small, water-occupied pores from which co-charge is efficiently excluded. Thus, the EC and TE potentials are dominated by exclusion ($\varepsilon = 1$ and $C_x(S_{wirr}) = C_x|_{ee}$). Conversely, at high water saturation, the water occupies most of the pores and the EC and TE potentials are dominated by diffusion ($\varepsilon$ is the minimum for the rock type of interest). At intermediate saturations, we model the saturation-dependence of the exclusion efficiency as (Jackson et al., 2012b)

$$\varepsilon_x = (1 - S_{wn})^3 \qquad (C.13)$$

where $\varepsilon_x$ is the ED or TE exclusion efficiency at intermediate saturation. Equation (C.13) was fitted to match the data presented in Ortiz et al. (1973) for the ED coupling coefficient, and we assume the same behavior for the TE relative coupling coefficient.

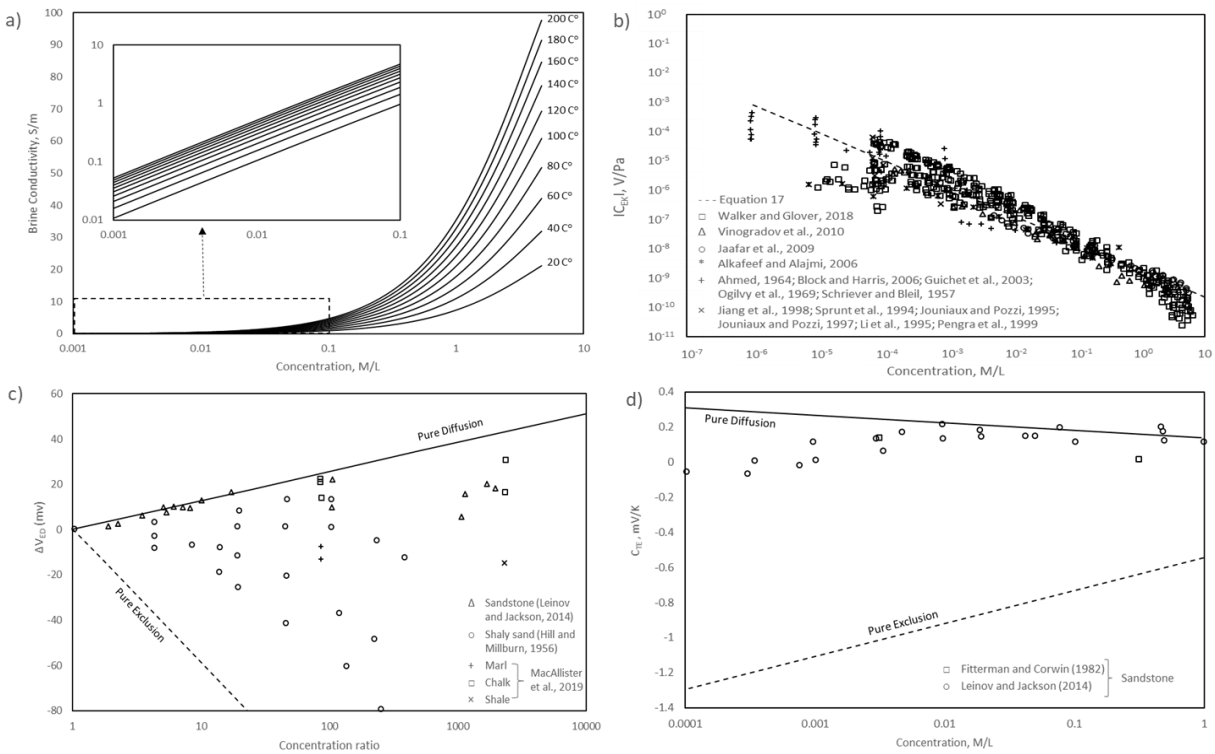


Figure C.1: a) Water conductivity versus brine concentration (ionic strength) at different temperatures. b) EK coupling coefficient versus brine concentration. c) ED coupling coefficient versus brine concentration ratio. d) TE coupling coefficient versus brine concentration.

## Appendix D

The algorithm path for the mldivide function for sparse matrices is given in figure D.1


Figure D.1: algorithm path for the mldivide function (MathWorks, 2020)

## References


Abdelrahman, E.S.M., Essa, K.S., Abo-Ezz, E.R., Sultan, M., Sauck, W.A. and Gharieb, A.G., 2008. New least-squares algorithm for model parameters estimation using self-potential anomalies. Computers & Geosciences, 34(11), 1569-1576.

Ahmad, M.U. 1964. A laboratory study of streaming potentials . Geophysical prospecting 12(1), 49–64.

Al Mahrouqi, D., Vinogradov, J., Jackson, M.D. 2017. Zeta potential of artificial and natural calcite in aqueous solution . Advances in colloid and interface science 240, 60–76.

Alkafeef, S.F, Alajmi, A.F. 2006. Streaming potentials and conductivities of reservoir rock cores in aqueous and non-aqueous liquids . Colloids and Surfaces A: Physicochemical and Engineering Aspects 289, 141–148.

Allègre, V., Lehmann, F., Ackerer, F., Jouniaux, L., Sailhac, P. 2012. A 1-D modelling of streaming potential dependence on water content during drainage experiment in sand . Geophysical Journal International 189(1), 285–295.

Angelis, M.D. 2005. Major ions in seawater . Water encyclopedia 4, 159–160.

Aziz, K., Settari, A. 1979. Petroleum Reservoir Simulation. Applied Science Publishers, London

Block, G.I., Harris, J,G. 2006. Conductivity dependence of seismoelectric wave phenomena in fluid-saturated sediments . Journal of Geophysical Research: Solid Earth 111, B01304.

Caglar, I.L., 2000. Visual interpretation of superposed self-potential anomalies in mineral exploration. Computers & geosciences, 26(7), 847-852.

Cherubini, Y., Cacace, M., Blöcher, G., Scheck-Wenderoth, M. 2013. Impact of single inclined faults on the fluid flow and heat transport: results from 3-D finite element simulations . Environmental earth sciences 70(8), 3603–3618.

Collini, H., Li, S., Jackson, M.D., Agenet, N., Rashid, B., Couves, J. 2020. Zeta potential in intact carbonates at reservoir conditions and its impact on oil recovery during controlled salinity waterflooding . Fuel 266, 116927.

Corwin, R.F., Hoover, D.B., 1979. The self-potential method in geothermal exploration . Geophysics 44(2), 226–245.

Darnet, M., Maineult, A., Marquis, G., 2004. On the origins of self-potential (SP) anomalies induced

by water injections into geothermal reservoirs . Geophysical Research Letters 31(19), L19609.

De Groot, S.R., Mazur, P., 1962. Non equilibrium thermodynamics, North-Holland Publishing Company: Amsterdam, pp 405-452.

DesRoches, A.J., Butler, K.E. and MacQuarrie, K.T., 2018. Surface self-potential patterns related to transmissive fracture trends during a water injection test. Geophysical Journal International, 212(3), 2047-2060.

Di Maio, R., Rani, P., Piegari, E. and Milano, L., 2016. Self-potential data inversion through a Genetic-Price algorithm. Computers & Geosciences, 94, 86-95.

Dilib, F.A. and Jackson, M.D., 2013. Closed-loop feedback control for production optimization of intelligent wells under uncertainty. SPE Production & Operations, 28(04), pp.345-357.

Dilib, F.A., Jackson, M.D., Mojaddam Zadeh, A., Aasheim, R., Årland, K., Gyllensten, A.J. and Erlandsen, S.M., 2015. Closed-loop feedback control in intelligent wells: application to a heterogeneous, thin oil-rim reservoir in the North Sea. SPE Reservoir Evaluation & Engineering, 18(01), pp.69-83.

Esmaeili, S., Rahbar, M., Pahlavanzadeh, H., Ayatollahi, S. 2016. Investigation of streaming potential coupling coefficients and zeta potential at low and high salinity conditions: Experimental and modeling approaches . Journal of Petroleum Science and Engineering 145, 137–147.

Fagerlund, F., Heinson, G., 2003. Detecting subsurface groundwater flow in fractured rock using self-potential (SP) methods . Environmental Geology 43(7), 782–794.

Fitterman, D.V., Corwin, R.F. 1982. Inversion of self-potential data from the Cerro Prieto geothermal field, Mexico . Geophysics 47(6), 938–945.

Ghommem, M., Qiu, X., Aidagulov, G., Abbad, M. 2018. Streaming potential measurements for downhole monitoring of reservoir fluid flows: A laboratory study . Journal of Petroleum Science and Engineering 161, 38–49.

Glover, P.W., Hole, M.J. and Pous, J., 2000. A modified Archie's law for two conducting phases. Earth and Planetary Science Letters, 180(3-4), 369-383.

Glover, P.W.J, Walker, E., Ruel, J., Tardif, E. 2012. Frequency-dependent streaming potential of porous media—Part 2: Experimental measurement of unconsolidated materials . International Journal of Geophysics 2012.

Glover, P.W.J., 2018. Modelling pH-dependent and microstructure-dependent streaming potential

coefficient and zeta potential of porous sandstones. Transport in Porous Media, 124(1), 31-56.

Gomes, J.L.M.A., Pavlidis, D., Salinas, P., Xie, Z., Percival, J.R., Melnikova, Y., Pain, C.C, Jackson, M.D. 2017. A force - balanced control volume finite element method for multi - phase porous media flow modelling . International Journal for Numerical Methods in Fluids 83(5), 431–445.

Graham, M.T., MacAllister, D.J., Vinogradov, J., Jackson, M.J., Butler, A.P., 2018. Self-Potential as a Predictor of Seawater Intrusion in Coastal Groundwater Boreholes . Water Resources Research 54(9), 6055-6071.

Guichet, X., Jouniaux, L., Pozzi, J.P. 2003. Streaming potential of a sand column in partial saturation conditions . Journal of Geophysical Research: Solid Earth 108(B3), 2141.

Gulamali, M.Y., Leinov, E., Jackson, M.D., 2011. Self-potential anomalies induced by water injection into hydrocarbon reservoirs . Geophysics 76(4), F283–F292.

Hill, H. J., Milburn, J.D. 1956. Effect of clay and water salinity on electrochemical behavior of reservoir rocks.

Hu, K., Jougnot, D., Huang, Q., Looms, M.C. and Linde, N., 2020. Advancing quantitative understanding of self-potential signatures in the critical zone through long-term monitoring. Journal of Hydrology, 124771.

Hunter, R.J, 1986. Zeta potential in colloid science . Academic press: New York.

Ijioma, A., 2016. Closed-loop feedback control of smart wells for production optimisation using self-potential measurements. Ph.D Dissertation, Imperial College London, London, United Kingdom.

Ishido, T., 2004. Electrokinetic mechanism for the “W”-shaped self-potential profile on volcanoes . Geophysical Research Letters 31(15), L15616–15619.

Ishido, T., Mizutani, H., 1981. Experimental and theoretical basis of electrokinetic phenomena in rock-water systems and its applications to geophysics . Journal of Geophysical Research: Solid Earth 86(B3), 1763–1775.

Jaafar, M.Z., Vinogradov, J., Jackson, M.D., 2009. Measurement of streaming potential coupling coefficient in sandstones saturated with high salinity NaCl brine . Geophysical Research Letters 36(21), L21306.

Jackson, D.M, , Gulamali, M, Leinov, L., Saunders, J., Vinogradov, J., 2010. Real-Time Measurements of Spontaneous Potential for Inflow Monitoring in Intelligent Wells . Proceedings SPE Annual Technical Conference and Exhibition. Society of Petroleum Engineers.

Jackson, M.D. 2015. 11.09- Tools and techniques: Self-potential methods, Treatise on geophysics (2nd ed.), Elsevier: Oxford, pp 261-293.

Jackson, M.D., 2010. Multiphase electrokinetic coupling: Insights into the impact of fluid and charge distribution at the pore scale from a bundle of capillary tubes model . Journal of Geophysical Research: Solid Earth 115(B7), B07206.

Jackson, M.D., Al-Mahrouqi, D., Vinogradov, J., 2016. Zeta potential in oil-water-carbonate systems and its impact on oil recovery during controlled salinity water-flooding . Scientific reports 6, 37363.

Jackson, M.D., Butler, A.P., Vinogradov, J., 2012a. Measurements of spontaneous potential in chalk with application to aquifer characterization in the southern UK . Quarterly Journal of Engineering Geology and Hydrogeology 45(4), 457–471.

Jackson, M.D., Gulamali, M.Y., Leinov, L., Saunders, J.H., Vinogradov, J., 2012b. Spontaneous potentials in hydrocarbon reservoirs during waterflooding: Application to water-front monitoring . SPE Journal 17(01), 53–69.

Jackson, M.D., Vinogradov, J. 2012. Impact of wettability on laboratory measurements of streaming potential in carbonates . Colloids and Surfaces A: Physicochemical and Engineering Aspects 393, 86–95.

Jiang, Y.G., Shan, F.K., Jin, H.M., Zhou, L.W., Sheng, P. 1998. A method for measuring electrokinetic coefficients of porous media and its potential application in hydrocarbon exploration . Geophysical Research Letters 25(10), 1581–1584.

Jougnot, D., Linde, N., Haarder, E.B. and Looms, M.C., 2015. Monitoring of saline tracer movement with vertically distributed self-potential measurements at the HOBE agricultural test site, Voulund, Denmark. Journal of Hydrology, 521, 314-327.

Jougnot, D., Linde, N., Revil, A., Doussan, C. 2012. Derivation of soil- specific streaming potential electrical parameters from hydrodynamic characteristics of partially saturated soils. Vadose Zone Journal, 11(1), 272– 286.

Jougnot, D., Roubinet, D., Guarracino, L. and Maineult, A., 2020. Modeling streaming potential in porous and fractured media, description and benefits of the effective excess charge density approach. In Advances in Modeling and Interpretation in Near Surface Geophysics (61-96). Springer, Cham.

Jouniaux, L., Pozzi, J.P. 1995. Streaming potential and permeability of saturated sandstones under

triaxial stress: Consequences for electrotelluric anomalies prior to earthquakes . Journal of Geophysical Research: Solid Earth 100(B6), 10197–10209.

Jouniaux, L., Pozzi, J.P. 1997. Laboratory measurements anomalous 0.1–0.5 Hz streaming potential under geochemical changes: Implications for electrotelluric precursors to earthquakes . Journal of Geophysical Research: Solid Earth 102(B7), 15335–15343.

Knipe, R.J., Jones, G., Fisher, Q.J. 1998. Faulting, fault sealing and fluid flow in hydrocarbon reservoirs: an introduction . Geological Society, London, Special Publications 147(1), vii–xxi.

Leinov, E., Jackson, M.D., 2014. Experimental measurements of the SP response to concentration and temperature gradients in sandstones with application to subsurface geophysical monitoring . Journal of Geophysical Research: Solid Earth 119(9), 6855–6876.

Leinov, E., Vinogradov, J., Jackson, M.D. 2010. Salinity dependence of the thermoelectric coupling coefficient in brine-saturated sandstones . Geophysical Research Letters 37(23), L23308.

Li, S., Collini, H., Jackson, M.D. 2018. Anomalous Zeta Potential Trends in Natural Sandstones . Geophysical Research Letters 45(11), 68–73.

Li, S.X., Pengra, D.B., Wong, P.Z. 1995. Onsager's reciprocal relation and the hydraulic permeability of porous media . Physical Review E 51(6), 5748-5751.

Lie, K.A. 2019. An introduction to reservoir simulation using MATLAB/GNU Octave: User guide for the MATLAB Reservoir Simulation Toolbox (MRST). Cambridge University Press.

Linde, N., Doetsch, J., Jougnot, D., Genoni, O., Duerst, Y., Minsley, B.J., Vogt, T., Pasquale, N. and Luster, J., 2011. Self-potential investigations of a gravel bar in a restored river corridor. Hydrology and Earth System Sciences, 15(3), 729-742.

Linde, N., Jougnot, D., Revil, A., Matthäi, S.K., Arora, T., Renard, D., Doussan, C. 2007. Streaming current generation in two-phase flow conditions . Geophysical Research Letters 34(3), L03306.

Linde, N., Revil, A., 2007. Inverting self-potential data for redox potentials of contaminant plumes. Geophysical Research Letters 34(14), L14302.

MacAllister, D.J., Graham, M.T., Vinogradov, J, Butler, A.P., Jackson, M.D. 2019. Characterizing the self-potential response to concentration gradients in heterogeneous subsurface environments . Journal of Geophysical Research: Solid Earth 124, 7918–7933.

MacAllister, D.J., Jackson, M.D., Butler, A.P., Vinogradov, J., 2018. Remote Detection of Saline Intrusion in a Coastal Aquifer Using Borehole Measurements of Self-Potential . Water

Resources Research 54(3), 1669–1687.

MathWorks. 2020. Matlab Function Reference. Available at: https://uk.mathworks.com/help/pdf_doc/matlab/matlab_ref.pdf

Minsley, B.J., Sogade, J., Morgan, F.D., 2007. Three-dimensional self-potential inversion for subsurface DNAPL contaminant detection at the Savannah River Site, South Carolina . Water Resources Research 43(4), W04429.

Murthy, I.R., Sudhakar, K.S. and Rao, P.R., 2005. A new method of interpreting self-potential anomalies of two-dimensional inclined sheets. Computers & geosciences, 31(5), 661-665.

Naudet, V., Revil, A, Bottero, J.-Y., Bégassat, P., 2003. Relationship between self-potential (SP) signals and redox conditions in contaminated groundwater . Geophysical research letters 30(21), 2091.

Naudet, V., Revil, A., Rizzo, E., Bottero, J.-Y., Bégassat, P., 2004. Groundwater redox conditions and conductivity in a contaminant plume from geoelectrical investigations. Hydrology and Earth System seiences 8(1), 8-22.

Numbere, D., Brigham, W.E., Standing, M.B. 1977. *Correlations for Physical Properties of petroleum reservoir Brines*. Stanford Univ., CA (USA). Petroleum Research Inst.

Nurafiqah, A., Hasan, N., Saeid, N., Mohyaldinn, M.E., Zahran, E.M.M. 2019. The study of the effect of fault transmissibility on the reservoir production using reservoir simulation—Cornea Field, Western Australia . Journal of Petroleum Exploration and Production Technology, 10, 739–753.

Ogilvy, A.A., Ayed, M.A., Bogoslovsky, V.A. 1969. Geophysical studies of water leakages from reservoirs . Geophysical Prospecting 17(1), 36–62.

Ortiz Jr ,I., Von Goten, W.D., Osoba, J.S., 1973. Relationship Of The Electorchemical Potential Of Porous Media With Hydrocarbon Saturation . The Log Analyst 14(02).

Pengra, D.B, Li, S.X., Wong, P.Z. 1999. Determination of rock properties by low-frequency AC electrokinetics . Journal of Geophysical Research: Solid Earth 104(B12), 29485–29508.

Perrier, F., Morat, P. 2000. Characterization of electrical daily variations induced by capillary flow in the non-saturated zone . Pure and Applied Geophysics 157(5), 785–810.

Peters, E., Arts, R.J., Brouwer, G.K., Geel, C.R., Cullick, S., Lorentzen R.J., Chen, Y., Dunlop, K.N.B., Vossepoel, F.C, Xu, R., Sarma, P., Alhutali, A.H., Reynolds, A.C. 2010. Results Of The Brugge Benchmark Study For Flooding Optimisation And History Matching. SPE Res Eval & Eng 13 (3): 391-405. SPE-119094-PA. doi: 10.2118/119094-PA.

Pruess, K., Oldenburg, C.M., Moridis, G.J. 1999. TOUGH2 user's guide version 2. Lawrence Berkeley National Lab.(LBNL), Berkeley, CA (United States).

Qu, D., Røe, P., Tveranger, J. 2015. A method for generating volumetric fault zone grids for pillar gridded reservoir models . Computers & Geosciences 81, 28–37.

Reppert, P.M., Morgan, F.D., 2003a. Temperature-dependent streaming potentials: 1. Theory . Journal of Geophysical Research: Solid Earth 108(B11),2546.

Reppert, P.M., Morgan, F.D., 2003b. Temperature-dependent streaming potentials: 2. Laboratory . Journal of Geophysical Research: Solid Earth 108(B11), 2547.

Revil, A. and Pezard, P.A., 1998. Streaming electrical potential anomaly along faults in geothermal areas. Geophysical Research Letters, 25(16), 3197-3200.

Revil, A. and Pezard, P.A., 1998. Streaming electrical potential anomaly along faults in geothermal areas. Geophysical Research Letters, 25(16), pp.3197-3200.

Revil, A., 1999. Ionic diffusivity, electrical conductivity, membrane and thermoelectric potentials in colloids and granular porous media: a unified model . Journal of Colloid and Interface Science 212(2), 503–522.

Revil, A., Cerepi, A., 2004. Streaming potentials in two-phase flow conditions . Geophysical Research Letters 31(11), L11605.

Revil, A., Karaoulis, M., Srivastava, S., Byrdina, S. 2013. Thermoelectric self-potential and resistivity data localize the burning front of underground coal fires . Geophysics 78(5), B259–B273.

Revil, A., Linde,N., Cerepi, A., Jougnot, D., Matthäi, S., Finsterle, S. 2007. Electrokinetic coupling in unsaturated porous media . Journal of colloid and interface science 313, 315–327.

Revil, A., Meyer, C.D., Niu, Q. 2016. A laboratory investigation of the thermoelectric effect . Geophysics 81(4), E243–E257.

Revil, A., Pezard, P.A., Glover, P.W.J., 1999a. Streaming potential in porous media: 1. Theory of the zeta potential . Journal of Geophysical Research 104(B9), 20021-20031.

Revil, A., Schwaeger, H., Cathles III, L.M., Manhardt, P.D., 1999b. Streaming potential in porous media: 2. Theory and application to geothermal systems . Journal of Geophysical Research: Solid Earth 104(B9), 20033–20048.

Roubinet, D., Linde, N., Jougnot, D. and Irving, J., 2016. Streaming potential modeling in fractured

rock: Insights into the identification of hydraulically active fractures. Geophysical Research Letters, 43(10), 4937-4944.

Rücker, C., Günther, T., Wagner, F.M., 2017. pyGIMLi: An open-source library for modelling and inversion in geophysics, Computers and Geosciences, 109, 106-123.

Saunders, J.H., Jackson, M.D., Gulamali, M.Y., Vinogradov, J., Pain, C.C., 2012. Streaming potentials at hydrocarbon reservoir conditions . Geophysics 77(1), E77–E90.

Saunders, J.H., Jackson, M.D., Pain, C.C., 2008. Fluid flow monitoring in oil fields using downhole measurements of electrokinetic potential . Geophysics 73(5), E165–E180.

Schlumberger. 2010. Eclipse reservoir simulator, manual and technical description. ECLIPSE technical description, version 10. Technical report.

Schriever, W., Bleil, C.E. 1957. Streaming potential in spherical-grain sands . Journal of the Electrochemical Society 104(3), 170-176.

Sen, P.N., Goode, P.A. 1992. Influence of temperature on electrical conductivity on shaly sands . Geophysics 57, 89–96.

Soldi, M., Jougnot, D., Guarracino, J. 2019. An analytical effective excess charge density model to predict the streaming potential generated by unsaturated flow . Geophysical Journal International 216, 380–394.

Soueid Ahmed, A., Jardani, A., Revil, A., & Dupont, J. P. (2013). SP2DINV: A 2D forward and inverse code for streaming potential problems. Computers & Geosciences, 59, 9-16.

Sprunt, E.S., Mercer, T.B., Djabbarah, N.F. 1994. Streaming potential from multiphase flow . Geophysics 59(5), 707–711.

Titov, K., Revil, A., Konosavsky, P., Straface, S., Troisi, S., 2005. Numerical modelling of self-potential signals associated with a pumping test experiment . Geophysical Journal International 162(2), 641–650.

Vinogradov, J., Jaafar, M.Z., Jackson, M,D., 2010. Measurement of streaming potential coupling coefficient in sandstones saturated with natural and artificial brines at high salinity . Journal of Geophysical Research: Solid Earth 115(B12), B12204.

Vinogradov, J., Jackson, M.D. 2015. Zeta potential in intact natural sandstones at elevated temperatures . Geophysical Research Letters 42(15), 6287–6294.

Vinogradov, J., Jackson, M.D., 2011. Multiphase streaming potential in sandstones saturated with gas/brine and oil/brine during drainage and imbibition . Geophysical Research Letters 38(1), L01301.

Vinogradov, J., Jackson, M.D., Chamerois, M.. 2018. Zeta potential in sandpacks: Effect of temperature, electrolyte pH, ionic strength and divalent cations . Colloids and Surfaces A: Physicochemical and Engineering Aspects 553, 259–271.

Voss, C.I., Provost, A.M. 2002. SUTRA: A model for 2D or 3D saturated-unsaturated, variable-density ground-water flow with solute or energy transport (No. 2002-4231).

Voytek, E.B., Barnard, H.R., Jougnot, D. and Singha, K., 2019. Transpiration-and precipitation-induced subsurface water flow observed using the self-potential method. Hydrological Processes, 33(13), 1784-1801.

Walker, E., Glover, P.W.J. 2018. Measurements of the relationship between microstructure, pH, and the streaming and zeta potentials of sandstones . Transport in Porous Media 121, 183–206.

Walker, E., Glover, P.W.J., Ruel, J., 2014. A transient method for measuring the DC streaming potential coefficient of porous and fractured rocks . Journal of Geophysical Research: Solid Earth 119(2), 957–970.

Wishart, D.N., Slater, L.D. and Gates, A.E., 2006. Self potential improves characterization of hydraulically-active fractures from azimuthal geoelectrical measurements. Geophysical Research Letters, 33(17).

Wurmstich, B., Morgan, F.D. 1994. Modeling of streaming potential responses caused by oil well pumping . Geophysics 59(1), 46–56.

Zhang, J., Vinogradov, J., Leinov, E., Jackson, M.D. 2017. Streaming potential during drainage and imbibition . Journal of Geophysical Research: Solid Earth 122(6), 4413–4435.

Zlotnicki, J., and Nishida, Y. 2003. Review on morphological insights of self-potential anomalies on volcanoes . Surveys in Geophysics 24(4), 291–338.